Atmospheric characterization of young L- and T-dwarfs

Bašić, Martina

Master's thesis / Diplomski rad

2024

Repository / Repozitorij:

Repository of Faculty of Science

University of Split

Faculty of Science

Atmospheric characterization of young L- and T- dwarfs

Master thesis

Martina Bašić

Split, rujan 2024.

Temeljna dokumentacijska kartica

Atmosferske karakteristike mladih patuljaka tipa L i T

Martina Bašić

Sveučilišni diplomski studij Fizika; smjer: Astrofizika i fizika elementarnih čestica

Sažetak:

Mladi smeđi patuljci sa spektralnim tipovima L i T prvenstveno emitiraju u bliskom infracrvenom području. Njihova raspodjela spektralne energije uvelike je pod utjecajem atmosferskih uvjeta, uključujući temperaturu, gravitaciju i kondenzaciju molekula. U ovom radu želimo odrediti efektivnu temperaturu i površinsku gravitaciju 34 smeđa patuljka smještenih u obližnjim mladim pokretnim skupinama i područjima stvaranja zvijezda. Karakteristike ovih objekata dobivene su usporedbom njihovih promatranih spektara, dobivenih instrumentom X-shooter na Vrlo velikom teleskopu (VLT-u), sa spektrima atmosferskih modela. Za usporedbu su korištena dva atmosferska modela: model ATMO bez oblaka i model BT-Settl-CIFIST s oblacima. Najbolje odgovarajuće vrijednosti efektivne temperature i površinske gravitacije za svaki objekt određene su metodom najmanjih kvadrata te su ti parametri korišteni za procjenu mase i radijusa. Analiza je pokazala da model BT-Settl-CIFIST preciznije odgovara spektrima L-tipova, dok je ATMO prikladniji za T-tipove patuljaka. Efektivne temperature općenito opadaju s kasnijim spektralnim tipovima, ali se uglavnom grupiraju oko 1800 K i 1700 K za objekte klasificirane između L0 i L5. Većina objekata ima mase iznad 3 M_J, što je očekivana donja granica za njihove spektralne tipove, iako neki padaju ispod ovog praga. Radijus objekata ovisi o faktoru razrjeđenja dobivenom usklađivanjem promatranog spektra i spektra modela spektra.

Atmospheric characterization of young L- and T- dwarfs

Martina Bašić

University graduate study Physics, specialization in Astrophysics and Elementary Particle Physics

Abstract:

Young brown dwarfs with L and T spectral types primarily emit in the near-infrared wavelengths. Their spectral energy distribution is heavily influenced by atmospheric conditions, including temperature, gravity, and molecule condensation. In this study, we aim to determine the effective temperature and surface gravity of 34 brown dwarfs located in nearby young moving groups and star-forming regions. We derived the characteristics of these objects by comparing their observed spectra, obtained with the X-shooter instrument on the VLT, to atmospheric model spectra. Two models were used for comparison: the cloudless ATMO model and the cloudy BT-Settl-CIFIST model. The best-fit effective temperature and surface gravity for each object were determined using the least squares method. These parameters were then used to estimate the mass and radius of the brown dwarfs. The analysis revealed that the BT-Settl-CIFIST model more accurately fits the spectra of L-type dwarfs, while the ATMO model is better suited for T-type dwarfs. The effective temperatures generally decrease with later spectral types but mostly cluster around 1800 K and 1700 K for objects classified between L0 and L5. Most objects have masses above 3 M_J, the expected lower mass limit for their spectral types, although some fall below this threshold. The radius of the objects depends on the dilution factor derived from matching the observed and model spectra.

Thesis is deposited in the library of the Faculty of Science, University of Split.

Contents

1   Introduction

Brown dwarfs are substellar objects with masses below 75 Jupiter masses (M_J), meaning they do not sustain hydrogen fusion. Ones with masses greater than 55 M_J can sustain lithium fusion, while those exceeding 13 M_J can burn deuterium [1]. In the early 1980s, the coldest known object was classified as an M8 dwarf, with a temperature of 2600 K, close to the lower mass limit for hydrogen burning at approximately 84 M_J. Technological advancements, particularly in near-infrared (NIR) photometry, enabled the detection of dimmer and cooler low-mass dwarfs, later termed 'brown dwarfs'. Due to their spectral characteristics, specifically the absence of the TiO absorption band found in M dwarfs, these objects could not be classified within the M-type. This led to the creation of a new classification, the L-dwarfs, while T-dwarfs were identified by the presence of prominent methane bands, which are not seen in L-dwarfs [2]. Due to the absence of hydrogen fusion in their cores, brown dwarfs cool continuously over time through thermal energy emission, spanning a wide temperature range across the L-, T-, and Y-type spectral classes. This cooling process results in degeneracies among mass, effective temperature, luminosity, and gravity, making these properties difficult to determine [3]. Observing and studying brown dwarfs is most effective in the NIR wavelength range [1 μm - 2.5 μm], where they emit the majority of their energy, representing the peak of their spectral energy distribution (SED). The various physical processes occurring within brown dwarfs influence the shape and characteristics of their spectra. Thus, a thorough analysis of their SED can provide a comprehensive understanding of their properties [2]. The atmosphere of a brown dwarf significantly affects its cooling rate and shapes the SED by imprinting the characteristics of gases, condensates, gravity, and temperature profiles onto the emitted radiation. It also plays a crucial role in determining the evolution and appearance of these objects. Accurately reproducing and interpreting the spectra of brown dwarfs is essential for understanding their characteristics, but this is challenging due to the complex role that condensate cloud formation plays at substellar atmospheric temperatures [4].

In the process of brown dwarf cooling, molecules form in their atmospheres, followed by condensates such as $Mg_2SiO_4, Ca_2SiO_4, MgTiO_3$ and Fe compounds. At lower temperatures, additional condensates form from substances that solidify or become semi-solid, under the cooler conditions present in these environments, such as H_2O, CH_4, NH_3 and CO_2. All those condensates create significant opacities that dominate the brown dwarfs' SED. Understanding the molecular opacities and the processes like condensation, sedimentation, coagulation, and convection that affect grain size distribution is essential for atmospheric modeling [5]. In L-dwarfs, dust forms in equilibrium, meaning the condensates are visible in the spectra and interact with the surrounding gas, even as the temperature drops. For T-dwarfs, rainout (sedimentation) chemistry is proposed, where reactions that would typically occur between condensed species and the gas are inhibited at temperatures below the condensation point, it can be envisioned as the condensate raining out of the atmosphere. Models incorporating dust

and clouds predict that cooler atmospheres, at T dwarf temperatures, are highly optically thick, leading to very shallow molecular bands in the spectra which would not even be possible in the cloudiest L-dwarfs. Therefore, T-dwarf spectra are then usually modeled using cloudless models, while L-dwarfs with models including dust and clouds [4].

Detailed and precise characterization of brown dwarfs provides an opportunity to study the physical and chemical processes occurring in gas giant planet atmospheres. The similarities in effective temperature and surface gravity between brown dwarfs and directly imaged planets offer valuable insights into the atmospheric properties and formation pathways of planetary-mass objects. These free-floating planetary-mass objects (PMOs) have masses below the deuterium-burning limit (<12 M_J) and, since they do not orbit a star, the degeneracies in the mass-luminosity relationship, along with their unknown age and distance, make it challenging to distinguish them from low-mass brown dwarfs [6]. PMOs gradually fade over time due to the absence of nuclear fusion in their cores, making them easier to observe when they are very young. Also it is crucial to observe them in regions where age and distance are well-known to minimize the effects of extinction and degeneracy. The primary regions for observing these objects are then nearby young moving groups (NYMGs) and nearby young star-forming regions (SFRs) [7].

In the work [8] 56 objects were identified from the mentioned regions as young brown dwarfs with L and T SpTs and were classified into specific sub-classes. The aim of this study is to determine the atmospheric properties of 34 of those objects, such as effective temperature, surface gravity, mass and radius, while also testing and evaluating the atmospheric models. Atmospheric characteriaztion consists of determining best-fit effective temperature and surface gravity by comparing the object spectrum to the model spectrum. Atmospheric models used for comparison are ATMO (cloudless) and BT-Settl-CIFIST (cloudy). In Section 2, we describe the dataset of the objects under analysis, highlight specific spectral lines for three objects across different SpTs, and explain the atmospheric models employed for characterizing these objects. Section 3 outlines the methodology used to determine the best-fit effective temperature (T_{eff}) and surface gravity ($\log g$) for each object, as well as the subsequent calculation of mass and radius using the determined T_{eff} and $\log g$, obtained from both models. In Section 4, we present a comparison of the results from the BT-Settl-CIFIST and ATMO models, focusing on the models' effectiveness and behavior when fitting the object spectra, as well as their mass and radius calculations. Finally, Section 5 provides the conclusions of the study.

2 Dataset and models

2.1 Sample of L- and T-dwarfs

The objects presented in this work, which we aim to characterize, were chosen from those classified in [8]. These objects are located in NYMG, SFRs, and clusters. These locations were selected due to the higher probability of finding relatively young objects, aged between 10 Myr and 600 Myr, spanning a large range of SpTs. In [8], a total of 56 objects were identified and classified into their SpTs, as detailed in Table A.2 of [8]. The scope of this work is to find the best-fit T_{eff} and log g of these objects by comparing their spectrum to the atmosphere models, and using those values to determine their mass and radius.

In Table 1 we present the groups in which these objects were found. Out of the 56 objects, we use 34 that are relevant to the goals of this study. We excluded objects belonging to the Upper Scorpius (USCO) group, due to extinction as an additional fitting parameter, and objects ID #51, #52, #53, #55, and #63. Objects ID #52, #55, and #63 are strong binary candidates with SpTs fitting combinations of L7+T7, L8+T6, and T2+T8, respectively. Objects ID #51 and #53 are classified as weak binary candidates with SpTs T1+T4 and T2+T4, respectively. The detection and classification process of binary candidates is explained in detail in [8].

The objects we analyze belong to M-, L-, and T-types: 2 objects of type M9, 30 objects of type L, and 2 objects of type T.

Table 1: *Ages of the groups of NYMGs, nearby young star forming regions (SFR) and clusters in which objects were found.*[1]

Region	Distance (pc)	Age (Myr)
ABDMG	30^{+20}_{-10}	149^{+51}_{-19}
ARG	72.4	$40 - 50$
BPMG	$30^{+20}_{-10}2$	24 ± 3
CARN	30 ± 20	200 ± 50
CAS	$5 - 20$	320 ± 80
COL	50 ± 20	42^{+6}_{-4}
THA	46^{+8}_{-6}	45 ± 4
TWA	60 ± 10	10 ± 3
32OR	96 ± 2	22^{+4}_{-3}
PLE	134 ± 9	112 ± 5
PRA	187.35 ± 3.89	600
USCO	145 ± 9	10 ± 3

---

[1]Table used from [8]

2.2 Spectral lines and molecular bands
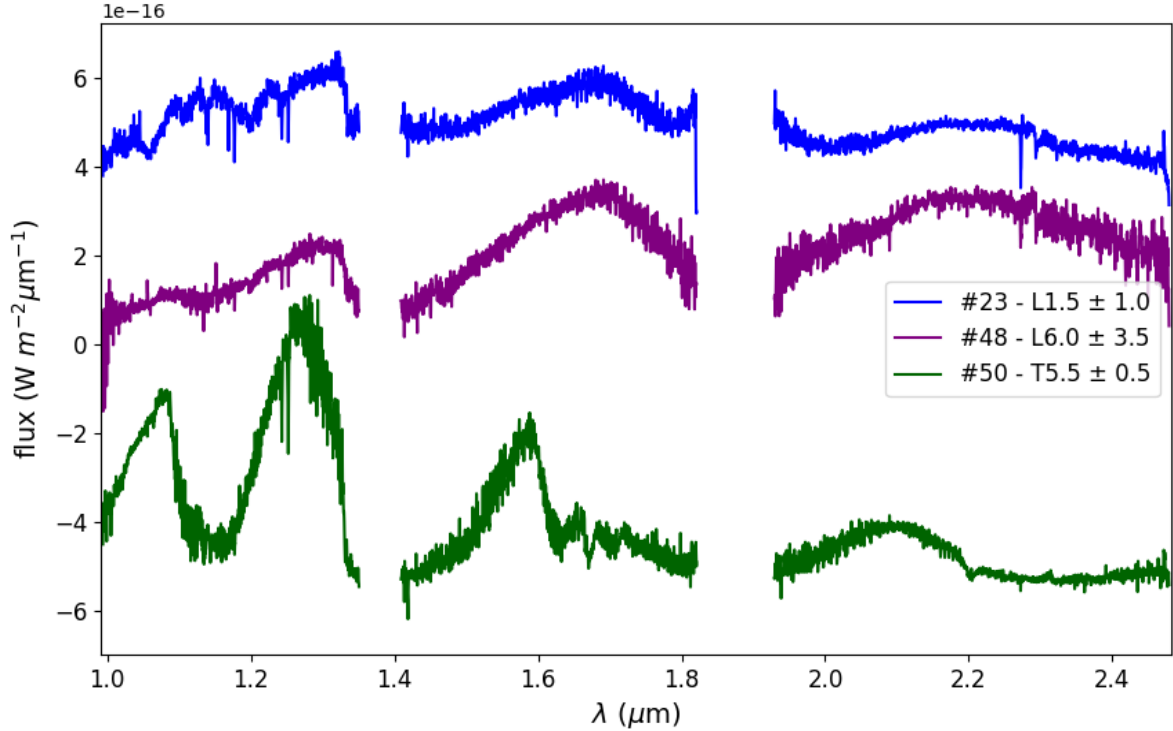
Figure 1: *Spectra of three objects from our sample with different SpTs. The overall shift in shape becomes noticeable as we progress to later spectral types (SpTs), for lower temperatures. Two breaks at wavelengths [1.35, 1.41] μm and [1.82,1.93] μm are due to absorption of light by Earth's atmosphere. Objects flux was normalized to the flux values of object ID #48 and plotted with an offset.*

The spectral classification of brown dwarfs relies on identifying specific spectral features. The presence or absence of certain atomic and molecular lines in the J-, H-, and K-bands allows for distinguishing M, L, and T-dwarfs and their subclasses. The wavelength ranges for the bands are [0.98, 1.35] μm (J-band), [1.41, 1.82] μm (H-band), and [1.93, 2.45] μm (K-band). In the short wavelengths of the J-band, the FeH line at 1.006 μm is prominent in M dwarf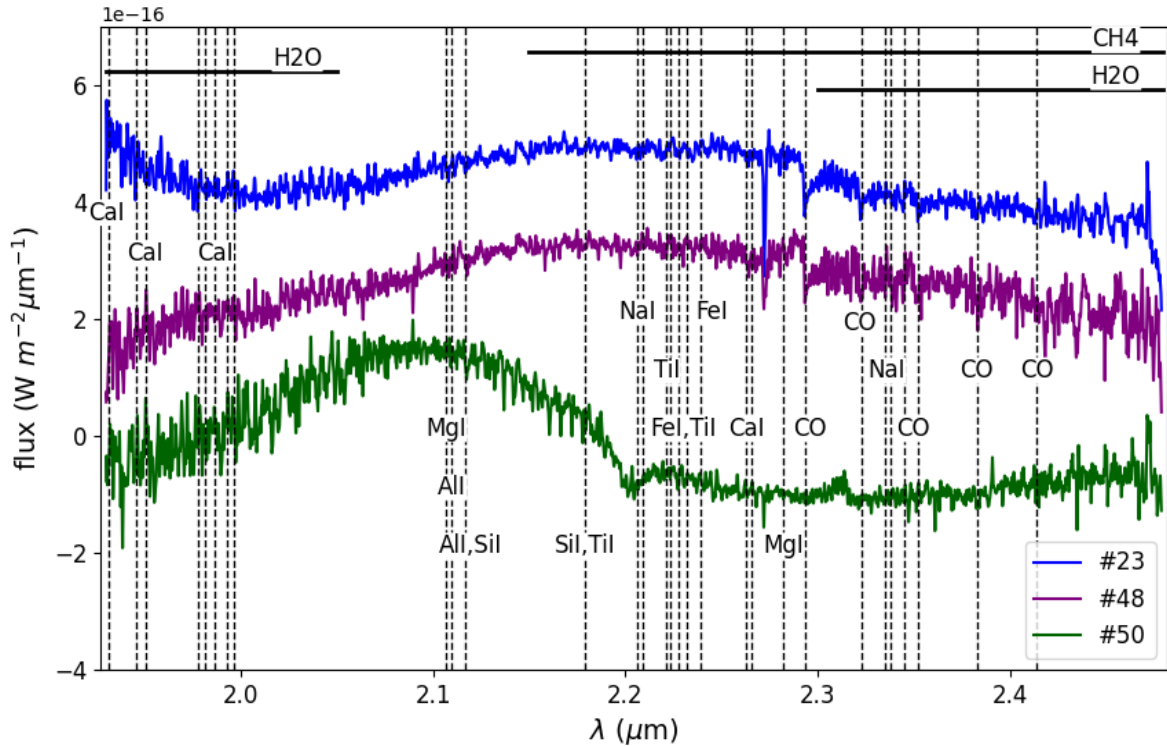s, diminishes towards L types, and disappears by SpT L7, but reappears in T5 dwarfs. The VO band, first visible in M5 dwarfs and peaking at M9, gradually fades towards L5. The most prominent lines in the J-band are the NaI doublet around 1.14 μm and the KI doublets around 1.175 and 1.25 μm. The FeI line at 1.189 μm is significant in M-type dwarfs and extends up to L5. M dwarfs exhibit a wider range of absorption lines including Mg, Ti, Si, and a notable abundance of FeI, while NaI and KI lines, along with three FeI lines around 1.155 μm, become more prevalent in later types beyond L1. The NaI doublet at 1.14 μm is visible up to L7, whereas KI lines extend throughout the T-dwarfs. Molecular bands of CH_4 and H_2O are associated with the peak formation of T-dwarfs at wavelengths around 1.27 μm. In the H-band, M dwarfs show distinct absorption lines for Mg, Si, K, and Al, which weaken in later M types and early L types, while the KI line at 1.516 μm is present up to L5. The CH_4 molecular band at 1.67 μm is characteristic of T-dwarfs and also appears in late L-dwarfs. In the K-band, weak NaI doublets around 2.21 and 2.34 μm and CaI around 1.95 μm are present in late M types

Figure 2: *Atomic lines and molecular bands stated in work [9] plotted over first part of spectrum for 3 objects: ID #23 with SpT of L1.5 (blue), #48 with SpT of L6.0 (purple), #50 with SpT of 5.5 (green). Objects flux was normalized to the flux values of object ID #48 and plotted with an offset.*

Figure 3: *Atomic lines and molecular bands stated in work [9] plotted over second part of spectrum for 3 objects: ID #23 with SpT of L1.5 (blue), #48 with SpT of L6.0 (purple), #50 with SpT of 5.5 (green). Objects flux was normalized to the flux values of object ID #48 and plotted with an offset.*

Figure 4: *Atomic lines and molecular bands stated in work [9] plotted over third part of spectrum for 3 objects: ID #23 with SpT of L1.5 (blue), #48 with SpT of L6.0 (purple), #50 with SpT of 5.5 (green). Objects flux was normalized to the flux values of object ID #48 and plotted with an offset.*

and L0. The prominent CO lines at 2.293, 2.323, 2.345, 2.352, 2.383, and 2.414 μm gradually disappear towards T2, with only the lines at 2.294 and 2.345 μm persisting. The H_2O band, which appears in M4 dwarfs, and the CH_4 band, which appears in late L types, both strengthen across the T-dwarf spectrum [9].

In this section, we provide a detailed illustration of the atomic and molecular bands, following the points and conclusions for young brown dwarfs form the work [9], for objects of our interest ID #23 (SpT L1.5 $\pm$ 1.0), ID #48 (SpT L6.0 $\pm$ 3.5), and ID #50 (SpT T5.5 $\pm$ 0.5). Object's flux can be divided into three wavelength regions, J-, H- and K-bands which will through the work be refereed as first, second and the third part of spectrum, respectively. Gaps in the spectrum, specifically in the ranges [1.35, 1.41] μm and [1.82, 1.93] μm, are due to light absorption by Earth's atmosphere. The J-, H- and K-bands will be zoomed in on for a detailed analysis of the data, as carried out in [10]. In Figure 1, we plot the spectra of the three objects to emphasize these gaps and the spectral changes that occur as the objects become cooler. The spectra are smoothed, normalized to the values of object ID #48, and plotted with an offset. To indicate the spectral lines and molecular bands present at different SpTs, we plot the three spectral parts of the objects, normalized and with an offset, with atomic lines and molecular bands corresponding to each wavelength range.

Figure 2 shows the J-band of the spectrum for the three objects. The FeH line is present in object #50 (SpT T5.5) and barely visible in object #48 (SpT L6), consistent with the findings

in [9], but is absent in object #23. The NaI doublet is visible in objects #23 and #48, being more prominent in #23 since it diminishes with later SpT and should be visible only up to type L7. The KI doublet at 1.25 μm is clearly visible in all three objects, while the one at 1.175 μm is more noticeable in #23 than in #48 and is absent in #50. The FeI line at 1.189 μm is barely visible in #23, while the FeI line at 1.155 μm, expected to be visible in all three objects, is also barely visible in #23 and #50. In Figure 3, which shows the H-band of the spectrum, we observe a weak absorption line of KI at 1.516 μm in object #23. There is a broad flux drop around 1.67 μm in #50, indicating a CH_4 absorption line. Figure 4 displays the K-band of the spectrum. The NaI doublets are not visible in object #23, even though it is an early L type (L1.5 $\pm$ 1.0). Object #23 exhibits all the expected CO absorption lines except those at 2.383 and 2.414 μm, while object #48 shows all except those at 2.323 and 2.414 μm. Object #50 does not show CO absorption lines, as expected for its SpT T5 classification. Additionally, a prominent CH_4 line around 2.27 μm is observed in all three objects.

2.3 Brown dwarf atmospheric models

Atmosphere models are critical tools for understanding the properties of brown dwarfs and exoplanets. They are implemented in codes designed to represent the complex three-dimensional structure of atmospheres. These models solve the radiative-convective flux processes occurring in brown dwarfs, producing the radiation emitted from the top of the atmosphere based on the internal heat flux. They consist of a grid spanning a range of T_{eff} and log g and emission spectra for each combination of T_{eff} and log g, which is used to compare with the observed spectra of objects. Each model employs a different strategy and parameter range to study the effects of cloud formation and the evolution of the objects. In this work, we consider two models, ATMO and BT-Settl-CIFIST (BSC), for comparison with the objects in our sample.

2.3.1 ATMO

The ATMO model is a cloudless model with a grid that spans a range of temperatures from 200 K to 3000 K, in 100 K increments, and surface gravities from log g = 2.5 to 5.5, with step of 0.5. However, its validity is limited to temperatures at and below 1900 K, as indicated by the authors in [3], because the model does not include opacity sources that form at higher temperatures, such as metal oxides and hydrides. This limitation means the model's predictions are less accurate at higher temperatures. The model comprises a pressure-temperature profile, chemical abundance profiles, and the flux emerging from the atmosphere. Chemical abundances are calculated for both dynamic equilibrium, where the atmosphere is unchanging, and non-equilibrium chemistry caused by convection in the atmosphere.

The ATMO opacity database includes 22 atomic and molecular species: $H_2 - H_2, H_2 - He$

(collision-induced dipoles), H^-, H_2O, CO_2, CO, CH_4, NH_3, Na, K, Li, Rb, Cs, Fe, TiO, VO, FeH, PH_3, HCN, C_2H_2, H_2S and SO_2. Non-equilibrium processes bring CO and N_2 to the upper atmosphere, where they become the dominant carbon and nitrogen species, while in equilibrium, the dominant species are NH_3 and CH_4. These chemical transitions are believed to cause convective instabilities in brown dwarfs and reddening of the spectrum [3].

2.3.2 BT-Settl-CIFIST

The BT-Settl model, implemented in the PHOENIX code [11], spans temperatures from 1200 K to 7000 K, in 100 K increments, but we limit it to 3000 K for efficiency, and surface gravities from 3.5 to 5.5, with step of 0.5. Dust formation and aerosol or dust clouds occur at temperatures below 2900 K, significantly impacting the NIR spectral energy distribution of late M-type and L-type atmospheres, which cover the temperature range from 1300 K to 2600 K. The BT-Settl model spans the entire temperature range and predicts the abundance of dust grains and granulation using non-gray radiative transfer, meaning the atmosphere is considered dynamical across all frequencies of stellar incident radiation [12].

The model is based on 55 species of grains and molecules, as listed in [12]. The size and distribution of these grains throughout the atmosphere depend on processes such as condensation, sedimentation, nucleation, and convective mixing. The version of the model used in this work, BSC, is an advanced version of the BT-Settl model. In [13], the authors specified more precise wavelengths for already known grains and incorporated solar chemical abundances into the PHOENIX code.

3 Data analysis method

The ATMO and BSC models present the dependence of flux on the wavelength at which it is emitted from an object at a specific T_{eff} and log g. The spectral types of the objects we are analyzing are mostly L- and T-types, thus we constrain the temperature of the models to values between 1200 K and 2600 K, as discussed in section 2.3. Given the age of the regions the objects come from, we constrain the log g to values of 4.0 and 4.5. Typically, for brown dwarfs, log g ranges from 3.5 for younger objects (<10 Myr) still in the process of gravitational contraction, to 5.0 for older objects in the field population with smaller radii due to the inverse relationship between radius and log g. The objects we are analyzing thus have log g values of 4.0, as they are older than 10 Myr, and 4.5, as we have young dwarfs from NYMG (Table A.2 in [8]).

To determine the specifications of the objects, such as mass and radius, we first need to determine atmospheric characteristics, temperature and gravity. These are found by comparing the observed spectra of the objects with the model spectra at different temperatures and gravity values. The best fit is determined using the least squares method.

3.1 Data preparation

The data for the objects consist of flux, wavelength, and noise, which represent the flux measurement errors. The first step in comparing the data with the models was to standardize the measurement units to those used by the models, which are, flux in $\frac{W}{m^2 \mu m}$, and wavelength in μm. The object's data for flux and noise was provided in units of $\frac{erg}{scm^2 \mathring{A}}$, and wavelength in nm. The conversion between units is given by $\frac{erg}{scm^2 \mathring{A}} = 10 \frac{W}{m^2 \mu m}$ and $nm = 1000 \, \mu m$.

Before finding the best fit using the least squares method, we also needed to mask the object spectra to remove 'not a number' values. Normalization of the model spectrum was necessary to compare them at the same flux values, and for this, a wavelength of 1.6 μm was used as the midpoint of the spectrum. For the three separate blocks of spectra, normalization was set at the middle of those spectral ranges: 1.2 μm, 1.6 μm, and 2.1 μm, respectively. The middle of the range was chosen as a normalization value cause it is mostly the neutral value of spectrum, without excessive peaks or drops. For each combination of temperature and gravity, resampling of the model spectrum was performed to ensure that the wavelength steps matched between the object and model flux, thereby obtaining the same data length for comparison.

The model spectra for both BSC and ATMO needed to be modified as described, but one additional step was required for the BSC model spectrum before resampling: convolution. Due to the resolution difference between the measured object spectrum and the model spectrum, the model spectrum had to be smoothed and reduced to match the object spectrum resolution, as specified in Table A.1 [8].

3.2 Least squares method

After adjusting the spectrum, the least squares method was used:

$$\chi^2 = \sum_i \frac{(O_i - M_i)^2}{\sigma_i^2},$$

(3.1)

where O_i is the value of object flux, M_i is the value of model flux, and σ_i is noise at each wavelength.

This value is determined for each combination of model temperature and gravity. T_{eff} and the log g corresponding to the minimum χ^2 value are chosen as the object's temperature and log g. In addition to determining the best-fit for the full spectrum of the objects, we also use the least squares method to find the best-fit T_{eff} and log g for each of the three parts of the spectrum for each object.

3.3 Calculation of mass and radius from dilution factor

The dilution factor C is a factor with which model spectrum needs to be multiplied to match the spectrum's absolutely callibrated flux and is also a value used to calculate the object's radius. In Section 3.1, we used normalization of the model spectrum to find the object's best-fit temperature. Here, we use the found T_{eff} and log g to calculate the dilution factor, which allows us to obtain the object's radius and then its mass.

Firstly, to calculate C we use the least squares method but in a different formulation than in the previous section. The formulation is as follows:

$$\chi^2 = \sum_i \frac{(O_i - C \cdot M_i)^2}{\sigma_i^2},$$

(3.2)

where O_i is the value of the object flux, M_i is the value of the model flux, and σ_i is the noise at each wavelength. The dilution factor C is determined by minimizing this χ^2 value as:

$$\frac{\partial \chi^2}{\partial C} = 0 \Rightarrow C = \frac{\sum_i \frac{M_i \cdot O_i}{\sigma_i^2}}{\sum_i \frac{M_i \cdot M_i}{\sigma_i^2}}.$$

(3.3)

Once C is calculated, it can be used to determine the object's radius R using the following relationship: $C = \left(\frac{R}{d}\right)^2 \Rightarrow R = d \cdot \sqrt{C}$, where $d = 1/p$ is the distance to the object, calculated from parallax p (Table 2, appendix A). With the radius R known, the mass M of the object can then be estimated using $M = gR^2/G$, where g is gravity, obtained from log g in units cm/s^2 and G is the gravitational constant.

4 Results

4.1 Effective temperatures
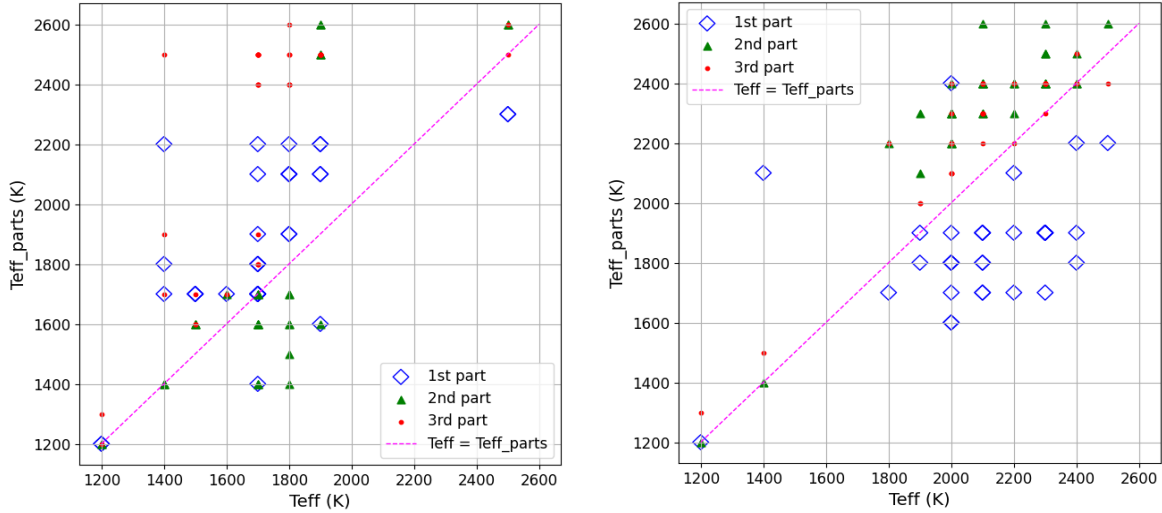
Figure 5: *Objects full spectrum best-fit* T_{eff} *(x-axis) compared to the best-fit* T_{eff} *for the parts of the spectrum (y-axis) shown for both of the models BSC (left) and ATMO (right). Blue diamonds represent the* T_{eff} *for the first part of the spectrum compared to the full spectrum, green triangles for the second part, and red dots for the third part. The magenta line represents the scenario where the best-fit temperature is consistent across the whole spectrum and its parts, depicted as the line y=x.*
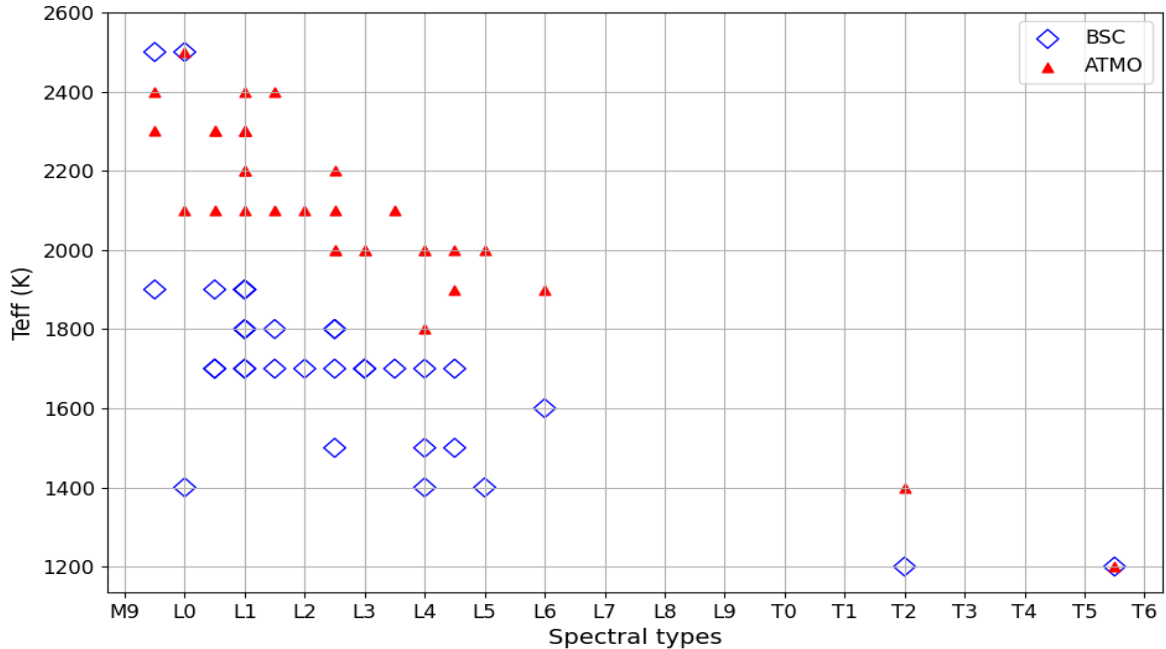
Figure 6: *Dependence of best-fit* T_{eff} *by BSC and ATMO models and SpT of the object. The uncertainties of the SpTs are omitted for clarity of the plot, but the assumed uncertainty of derived* T_{eff} *is 100 K. The BC model SpT-*T_{eff} *dependence is plotted in blue diamonds, and ATMO in red squares.*

In appendix B we present the best-fit temperatures obtained from comparing each object with the ATMO and BSC models, with an expected error of ± 100 K for each fit defined by the

model grid spacing. Figure 5 displays the temperature dependence for the full spectrum and all three parts of the spectrum: BSC model on the left and ATMO on the right. Best-fit T_{eff} for the three parts of spectrum is plotted with diamond, triangle and a circle, respectively, and a dashed magenta line is added to indicate $x = y$ relation. These visuals are intended for observing temperature behaviors to extract general model trends; object IDs are omitted as they are not the focus of these plots.

From the Figure 5 it is evident that the BSC model shows one object aligned with the magenta line at 1200 K and another object with two parts matching the full spectrum temperature at 1700 K. The model tends to predict slightly higher temperatures for the first part of the spectrum compared to the full spectrum, with a mean difference of approximately 210 K. Mean difference was calculated for each part of the spectra using all best-fit T_{eff} (Table 3) to quantify the deviation from the full spectrum best-fit. For the second part, best-fit temperatures cluster around the magenta line at a median of 1800 K, with a mean difference of 190 K. The third part of the spectrum displays a split: a smaller cluster around 1800 K and a larger one at higher temperatures on the y-axis, resulting in a mean difference of about 490 K. This analysis suggests that the BSC model may slightly misalign when zooming into the third part of the spectrum for objects in the higher temperature cluster, while providing a fair match for those closer to the magenta line and for the first and second part of the spectrum.

The ATMO model does not align any objects precisely with the magenta line and has two objects with two parts of the spectrum at the same temperatures as the full spectrum: 1200 K and 2400 K. For the first part of the spectrum, the model tends to select best-fit temperatures around 1800 K, with a mean difference of 320 K, although the full spectrum best-fit often exceeds 2000 K. The second and third parts of the spectrum predominantly show best-fit temperatures above 2000 K, with the second part having a mean difference of 210 K and the third part showing the smallest difference of 150 K. This pattern suggests that the ATMO model tends to underestimate best-fit temperatures for the first part of the spectrum, while generally aligning with or slightly exceeding the full spectrum temperatures in the second and third parts.

In Figure 6, we present the dependence of best-fit T_{eff} on the SpTs of the objects for the full spectrum. The BSC model best-fits, plotted with blue diamonds, cluster around 1700 K and span a wide range of L SpT types, from early L0 to mid-type L5. Most BSC model T_{eff} values are in the mid to lower temperature range ($T_{eff} < 1900$ K) across all SpTs, with two objects exhibiting a higher temperature of 2300 K. As the spectral types approach mid-L types ($< L3$), more objects have lower T_{eff} (< 1700 K) compared to the objects of SpT L0, L1, L2, and L3. For the two T-type objects, the best-fit T_{eff} is 1200 K. The ATMO model, on the other hand, shows higher T_{eff} values of 2000 K and 2100 K for a wide range of L SpT types. Higher T_{eff} values correspond to the earlier L types, while lower values correspond to the later L types, showing a roughly linear decrease. The object with SpT T2 has a best-fit T_{eff} of 1400 K, while the object with SpT T5.5 has a best-fit T_{eff} of 1200 K. From this comparison we see that both models have similar best-fit T_{eff} for T-type objects, but the effectiveness of the model depends

on the spctra matching. So in the next section, we will compare the spectra for both the BSC and ATMO models for the object ID #50 with a SpT of T5.5 and T_{eff} 1200 K and demonstrate that the ATMO model provides a better match with the object's spectrum.

The results we obtained in Figure 6 align with those presented in the work [14]. As we see in Figure 6 the BSC model indeed shows a gap in temperatures between 2000 K and 2400 K, and a concentration of late L types and transition M/L types at 1700-1800 K. Due to the error value for the SpTs, objects classified as L0-2 span the M/L transition range. In this M/L transition, as T_{eff} decreases, there is an increase in cloud opacity. The temperature gap between 2000 K and 2400 K likely results from the BSC model's inadequate incorporation of dust in that T_{eff} range. The accumulation of later L-type objects may be influenced by the BSC model's over-prediction of dust, which tends to increase slightly towards later L-type objects [14].

4.2 Model comparison

For a detailed interpretation and study, we selected 4 objects out of 34, each with different SpT, to demonstrate the best-fit T_{eff} differences and model behavior. The chosen objects are: ID #36 SpT L1.5±1.0, #21 and #47 same SpT L4.5±3.0 and object ID #50 SpT T5.5±0.5. The plots shown in the next subsections display the full spectrum for the best-fit and log g for both models used, ATMO and BSC, as well as three separate best-fit spectra. The observed data is plotted in gray, the BSC model in blue, and the ATMO model in red.

4.2.1 Object Id #36
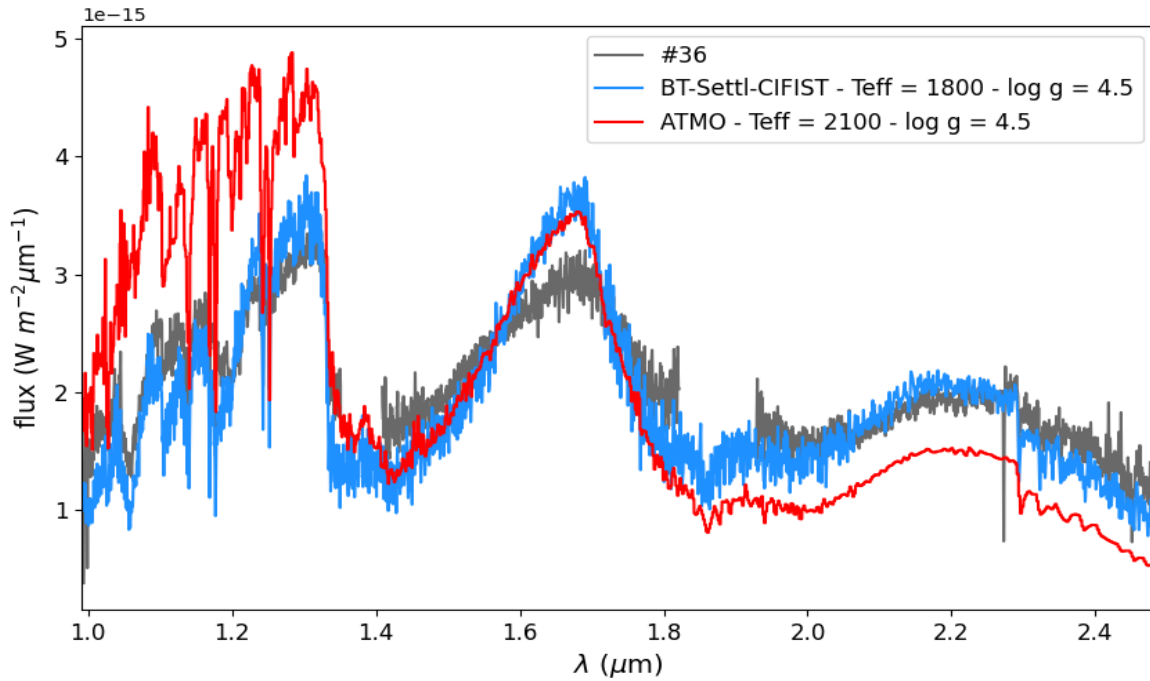
Figure 7: *The spectrum of object ID #36 (shown in gray) is compared with the best-fit T_{eff} and log g values from the BSC model (depicted in blue) and the ATMO model (depicted in red). The fitting process covered the entire spectral range.*

Figure 7 shows the full object spectrum along with the ATMO and BSC model spectra at their best-fit T_{eff} and log g values. The BSC model's best-fit T_{eff} is 1800 K and log g is 4.5, resulting in an object radius of 1.41 ± 0.03 R$_J$ and a mass of 24.4 ± 28.1 M$_J$. In Figure 7, the width of the model curve in the second part of spectrum is more narrow than that of the object, having higher flux values than the object in the peak and lower it at the tails of the curve. For the first and third parts it slightly underpredicts the flux. The ATMO model's full spectrum best-fit T_{eff} is 2100 K with log g of 4.5, giving a radius of 0.97 ± 0.02 R$_J$ and a mass of 11.5 ± 13.3 M$_J$. In Figure 7, the second part of the model's spectrum behaves similarly to the BSC model up until 1.8 μm, where it significantly underpredicts the object's flux values, continuing this trend in the
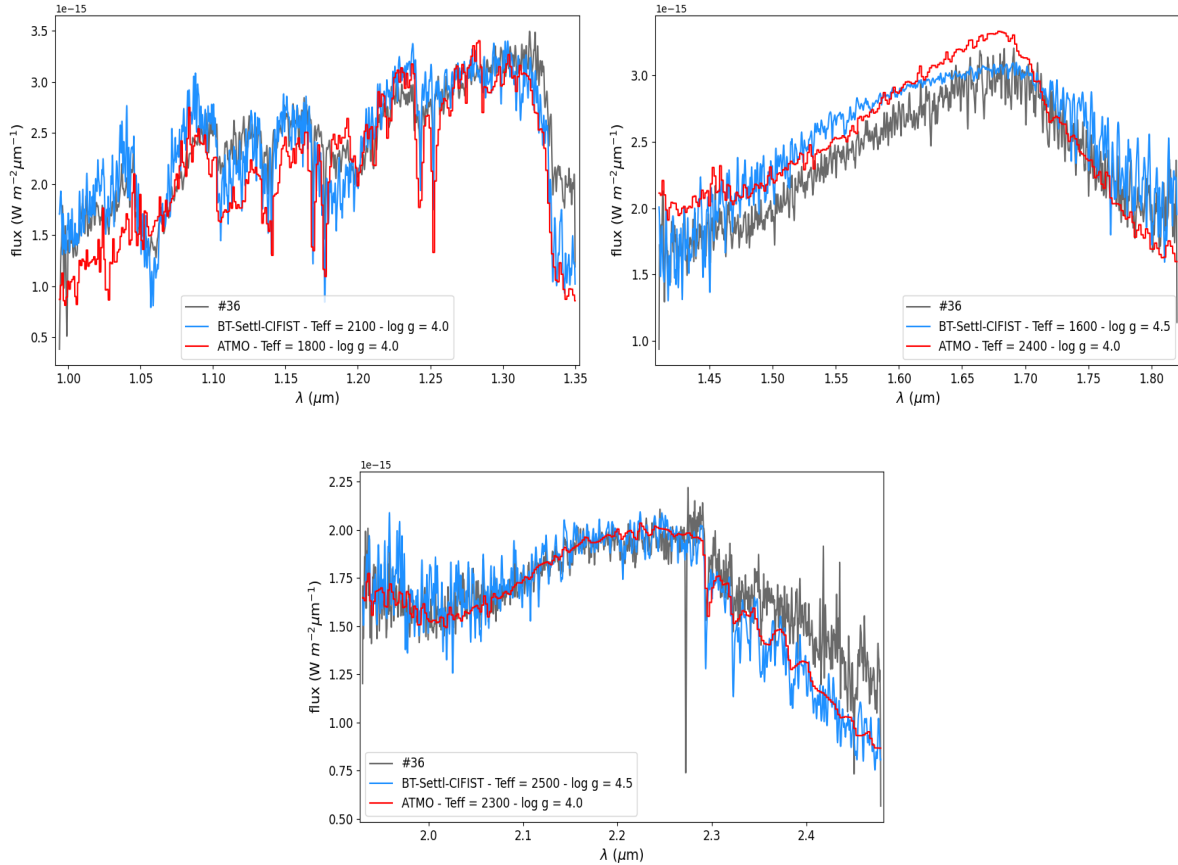
Figure 8: *Three parts of spectrum of object ID #36 shown and fitted separately with best-fits BSC (blue) and ATMO (red) models.*

third part of the spectrum. In the first part, it displays considerably higher flux values than the object spectrum until around 1.3 μm, where it shows an abrupt decline.

Figure 8 shows zoomed-in views of the three parts of the spectrum and their separate best-fit temperatures for the BSC and ATMO model. The BSC model for the first part has the best-fit T_{eff} higher than that of the full spectrum at 2100 K with log g of 4.0, providing a better fit than for the full spectrum with slight divergence in the wavelength range [1.3, 1.35] μm. The second part's best-fit T_{eff} is 1600 K, with a gentler slope than the object's. The BSC model does not show a peak in the wavelength range [1.65, 1.7] μm at these temperatures and over-predicts the flux at the end of the second part. The bottom image of Figure 8 shows the third part of the spectrum at a best-fit T_{eff} of 2500 K, which is the highest best-fit T_{eff} for this object. In the range [1.93, 2.3] μm, the model very well matches the object's spectrum but exhibits a steeper decline in the latter range of the third part. Based on the conclusions in Section 4.1, the BSC model fits well with the object's spectrum for the second and third parts, although the third part has a high divergence of best-fit T_{eff} from the full spectrum best-fit. ATMO model's best-fit T_{eff} for all three parts of the spectrum are 1800 K, 2400 K, and 2300 K, respectively. In the first part of the spectrum, the model has slightly lower flux values than the object, while in the second part, it has higher flux values, but the slope matches the object's, with a peak in the wavelength

15

range [1.65, 1.7] μm. The third part of the spectrum matches the one for the BSC model but at a 100 K lower temperature. From the T_{eff} analysis for the ATMO model in Section 4.1, this object indeed has the best-fit T_{eff} for the first part at 1800 K, while the second and third parts are in a higher T_{eff} range and show acceptable matching with the object's spectrum.

The BSC model offers a more accurate overall fit for this object at a T_{eff} of 1800 K and a log g of 4.5, except in the second part of the spectrum, where it overestimates the peak. This discrepancy is likely due to insufficient dust opacity in the model, which becomes particularly noticeable during the M/L transition phase, where our object is classified. This observation aligns with the findings reported in [15].

4.2.2 Object Id #21
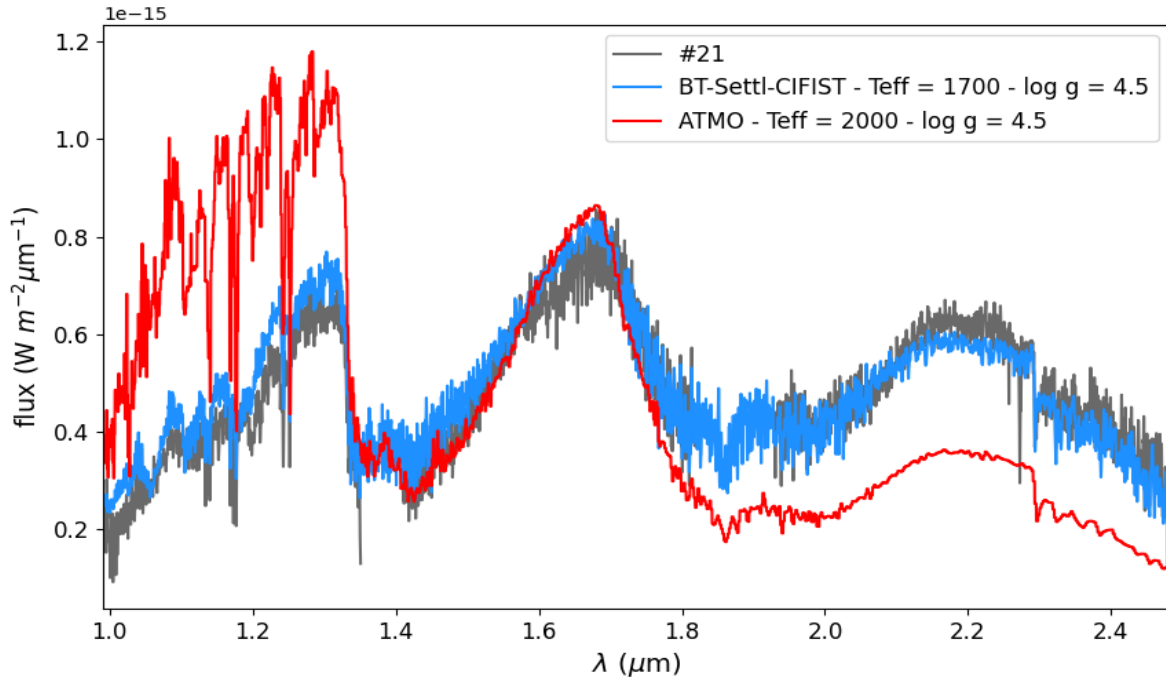
Figure 9: *The spectrum of object ID #21 (shown in gray) is compared with the best-fit T_{eff} and log g values from the BSC model (depicted in blue) and the ATMO model (depicted in red). The fitting process covered the entire spectral range.*

The BSC model's best-fit T_{eff} is 1700 K and log g is 4.5, resulting in an object radius of 0.7 ± 0.02 R_J and a mass of 5.8 ± 6.7 M_J. In Figure 9 we see that BSC model flux values approximately align with the objects. In the second part of spectrum, the model values overlap with the object's, except in a small range around wavelength 1.6 μm, at the peak curve values. At this T_{eff}, the model over-predicts the flux values in the range [0.98,1.35] μm while in the transition between the first and the second part of spectrum, during the flux value drop, it corresponds well with the object's spectrum. The third part of spectrum aligns with the object at the begging of the range, but the latter flux values are slightly lower than the object's. On
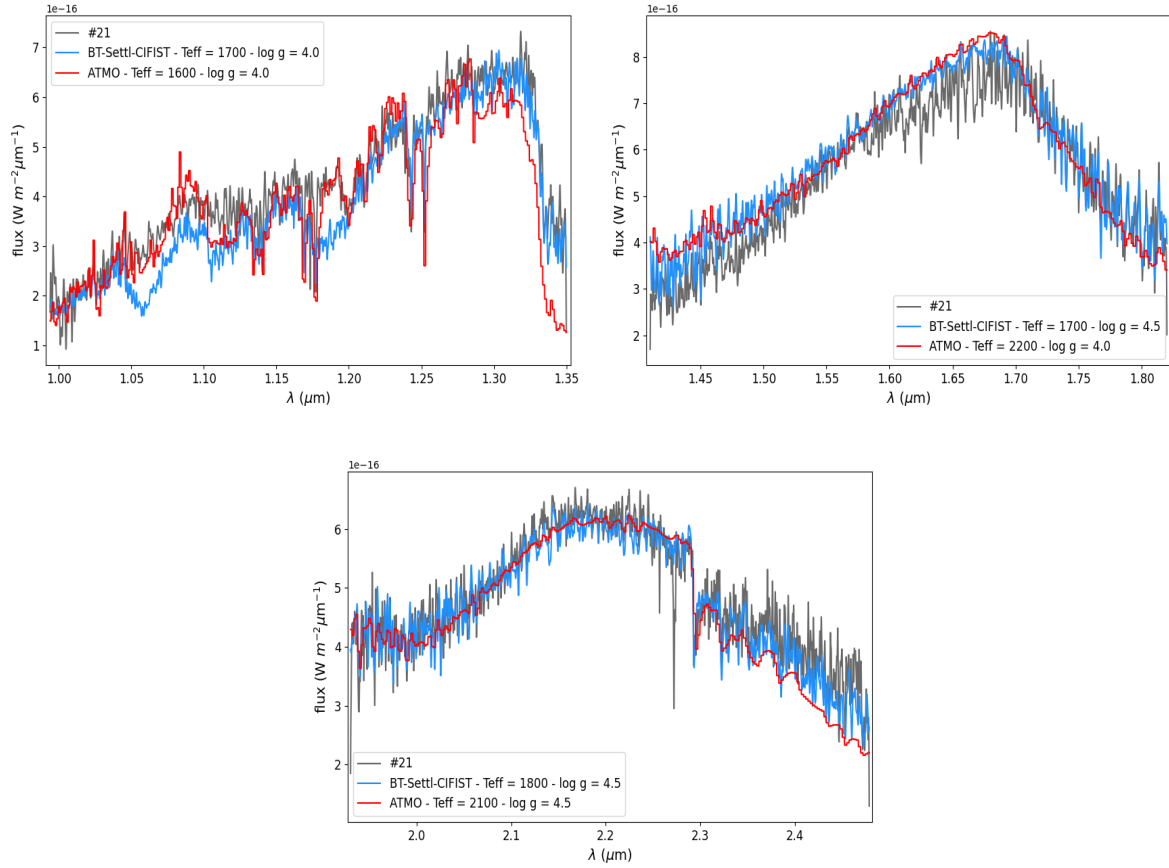
Figure 10: *Three parts of spectrum of object ID #21 shown and fitted separately with best-fits BSC (blue) and ATMO (red) models.*

the other hand, the ATMO model's best fit T_{eff} is 2000 K and log g is 4.5, which gives the objects radius as 0.44 ± 0.01 R_J and mass of 2.3 ± 2.7 M_J. In Figure 9, the ATMO model gives exceptionally high flux values for the first part of spectra, only to have a steep fall at wavelength value of approximately 1.35 μm and align with the object spectra at the begging of the second part of spectrum. At this T_{eff} the ATMO model has a higher peak at an shorter wavelength than the object, causing a mismatch, and shows lower flux values continuing into the third part of the spectrum.

In Figure 10 we show the zoomed in three parts of spectra for both models. The BSC model best-fit for the first two parts of spectrum is the same as the full spectrum BSC best fit at 1700 K, while the third part best-fit is 1800 K, within the expected T_{eff} error of 100 K. Figure 10 shows that BSC model somewhat underpredicts the flux values in the first part of spectrum, while in the second part, it slightly over-predicts the flux values, especially at the curve peak. An excellent match between the object and the model is evident in the wavelength ranges [1.3, 1.35] μm and [1.93,2.25] μm. The ATMO model gives a better match with the first part of spectrum at 1600 K than BSC model, but has a more abrupt and deeper fall in flux values at the far end. For the second and the third parts of spectrum, the best-fit T_{eff} is 2200 K and 2100 K, respectively, which is similar to the full spectrum best-fit. However, it shows misalignment in

both parts, with a slight match at the beginning of the third part.

For this object, the BSC model provides an excellent match with the object's spectrum at a T_{eff} of 1700 K and a log g of 4.5. In contrast, the ATMO model does not accurately replicate the object's spectrum, except for the first part, which was fitted separately.

4.2.3 Object Id #47
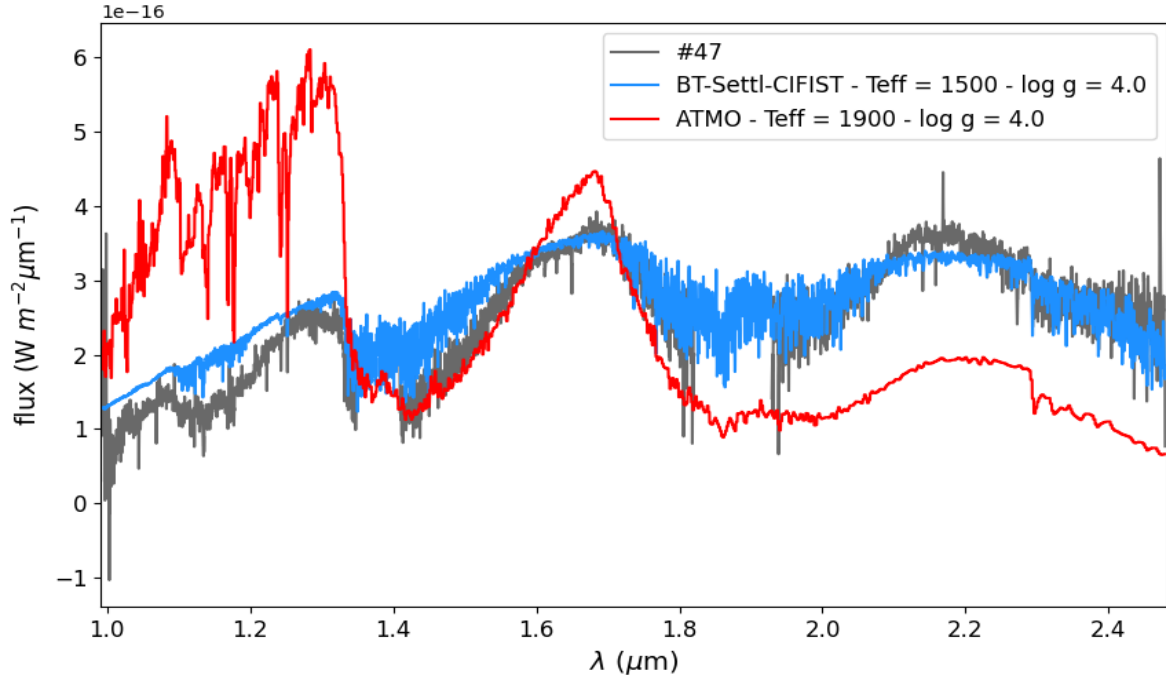
Figure 11: *The spectrum of object ID #47 (shown in gray) is compared with the best-fit T_{eff} and log g values from the BSC model (depicted in blue) and the ATMO model (depicted in red). The fitting process covered the entire spectral range.*

From Figure 11, we observe that the object's spectrum is flatter with lower amplitudes compared to the other objects. The BSC model's best-fit T_{eff} is 1500 K, slightly lower than that of object ID #21 with the same SpT, and the log g of 4.0. Due to the lack of distance measurement, it was not possible to calculate the mass and the radius for this object. Although the BSC model does not fully overlap with the object spectrum, it provides a close approximation. At the best-fit T_{eff} and log g the model curve is flatter than the object's, making it difficult to fit the irregularities in the object spectrum. The first part of the object spectrum shows a slight decrease in flux values around 1.2 μm, while the model's flux remains relatively constant, consistently having higher values. In the second part, the model spectrum does not exhibit the slight peak seen in the object spectrum around 1.7 μm, resulting in lower flux values in that region, and it has a wider curvature, causing the model to over-predict the flux values at the tails. Similarly, the third part of the spectrum lacks the model peak around 2.2 μm. The flattening of the BSC model flux is a consistent occurance for $1300 < T_{eff} < 1700$
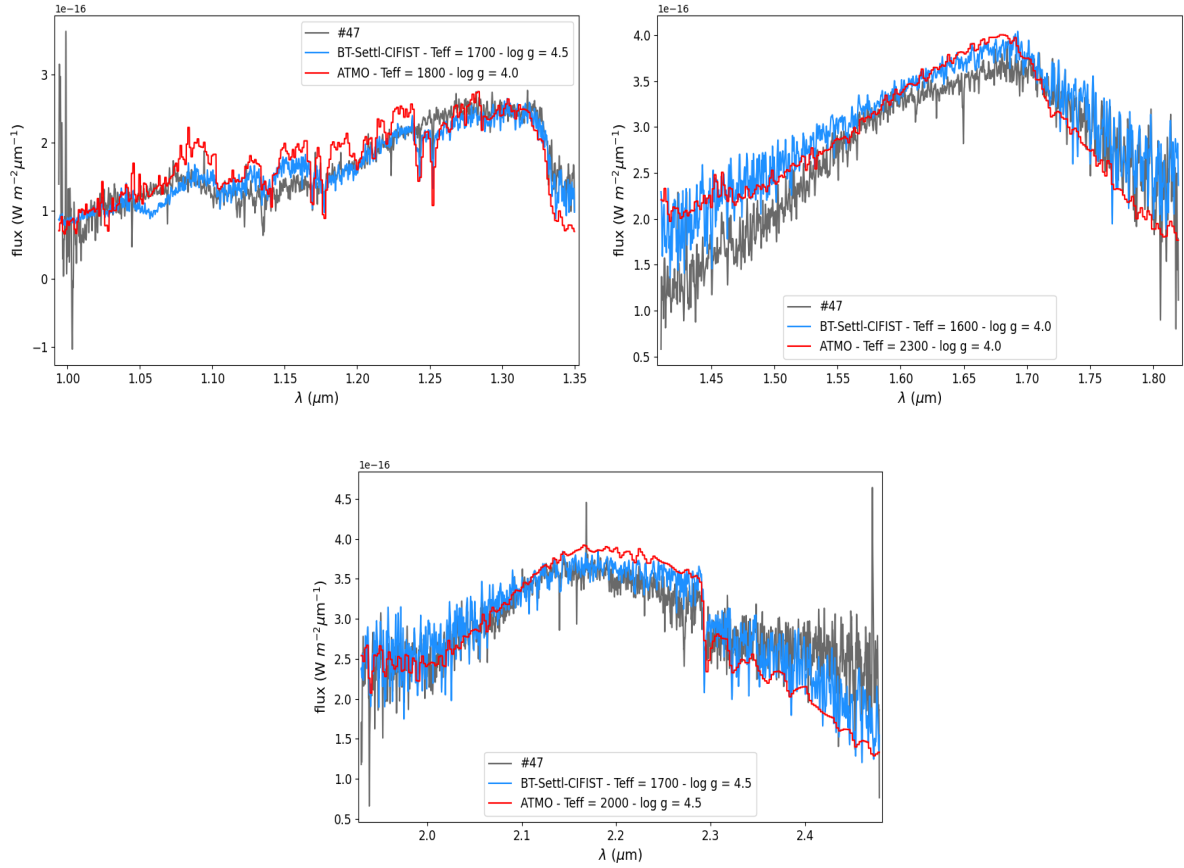
Figure 12: *Three parts of spectrum of object ID #47 shown and fitted separately with best-fits BSC (blue) and ATMO (red) models.*

K with the log *g* value 4.0, and only a few analyzed objects have this log *g* value, resulting in a flatter spectrum especially in the first part. The ATMO model does not show flattening in the spectrum, regardless of differen T_{eff} or log *g* values. This affects the mismatch of the model's full spectrum best-fit with the object's spectrum, shown in Figure 12 at T_{eff} 1900 K and log *g* 4.0. Due to the significant model flux peak in the second part of the spectrum at around 1.7μm and the narrow curvature, the decrease in flux values continues in the third part, underpredicting the flux values at larger wavelengths. This model consistently over-predicts flux values in the first part of the spectrum and underpredicts them in the third part at higher object T_{eff}, as explained in Section 2.3.1.

In Figure 12, the best-fit T_{eff} and log *g* for parts of the spectrum for the BSC model are 1700 K and 4.5, 1600 K and 4.0, and 1700 K and 4.5, respectively. These values are relatively close to the best-fit for the full spectrum of 1500 K. The model spectrum for the first and third parts of the spectrum has a relatively good match with the object spectrum, with slight divergence, while the second part of the model spectrum, which is the only one at 1600 K, has a slight misalignment. In the second part, the object spectrum has a sharper rise to the peak values around 1.65 μm than the model flux, but the decline to end at wavelength 1.85 μm matches well. The ATMO model's best-fits for parts of spectrum are also at higher T_{eff} values than the

19

full spectrum best-fit. Although the three parts have a better match than the full spectrum, there are still many inconsistencies between the object and ATMO model spectrum. For the full spectrum best-fit, the ATMO model gives a highly mismatched fit, while the BSC model provides a somewhat close match at T_{eff} of 1500 K.

4.2.4 Object Id #50
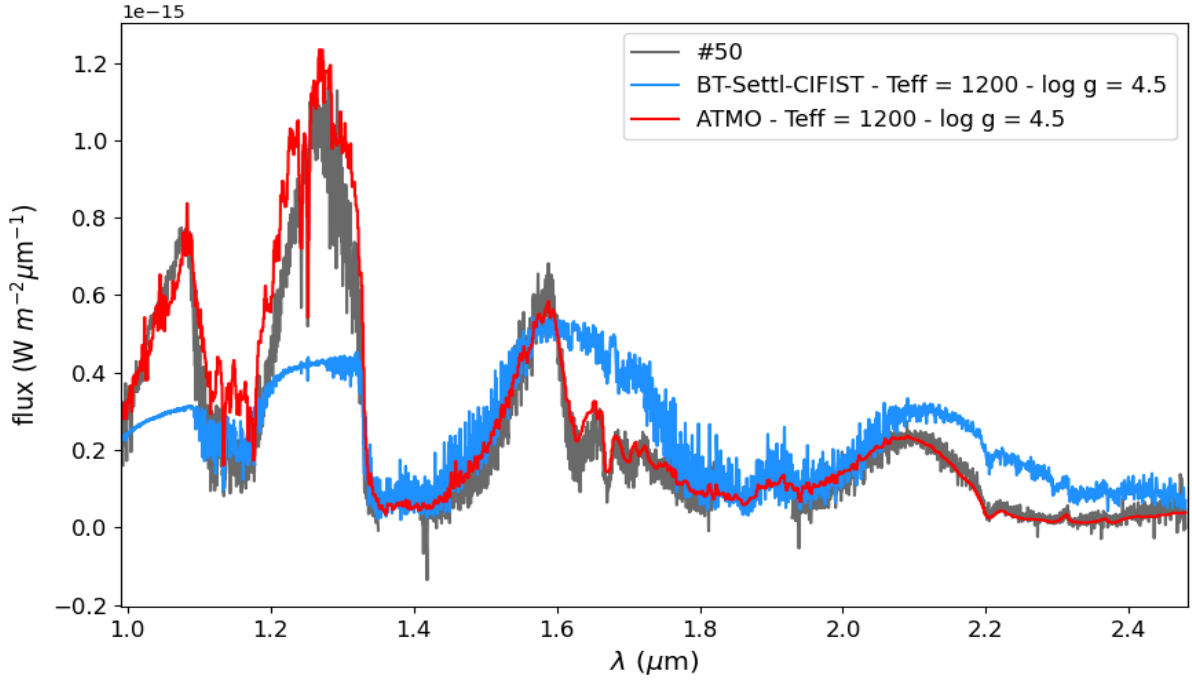
Figure 13: *The spectrum of object ID #50 (shown in gray) is compared with the best-fit T_{eff} and log g values from the BSC model (depicted in blue) and the ATMO model (depicted in red). The fitting process covered the entire spectral range.*

This is the only object whose full spectrum best-fit T_{eff} for both models, ATMO and BSC, is 1200 K and same log g 4.5. The BSC model radius is 0.52 ± 0.01 R_J and mass 3.3 ± 3.8 M_J, while ATMO model radius is 0.52 ± 0.01 R_J and mass 3.3 ± 3.8 M_J. The slight difference between the mass and radius for the models with same T_{eff} and log g lays in the different values of dilution factor C. From Figure 13 we see the full spectrum and the fit difference between the models. The object's spectrum features three distinctive peaks at wavelengths around 1.15, 1.25 and 1.6 μm, with a smaller peak at 2.1 μm. The BSC model fails to reproduce these peaks, instead displaying weak curves at those wavelengths that do not reach the high flux values observed in the object's spectrum, although the curve widths are similar. There is significant underprediction of flux in the first part of the spectrum and over-prediction in the latter wavelengths. Additionally, the model does not show a peak around 1.6 μm, but rather a weak curve with a gentler right tail compared to the object. Conversely, the ATMO model matches the object's spectrum excellently, replicating the peaks and flux drops at the same
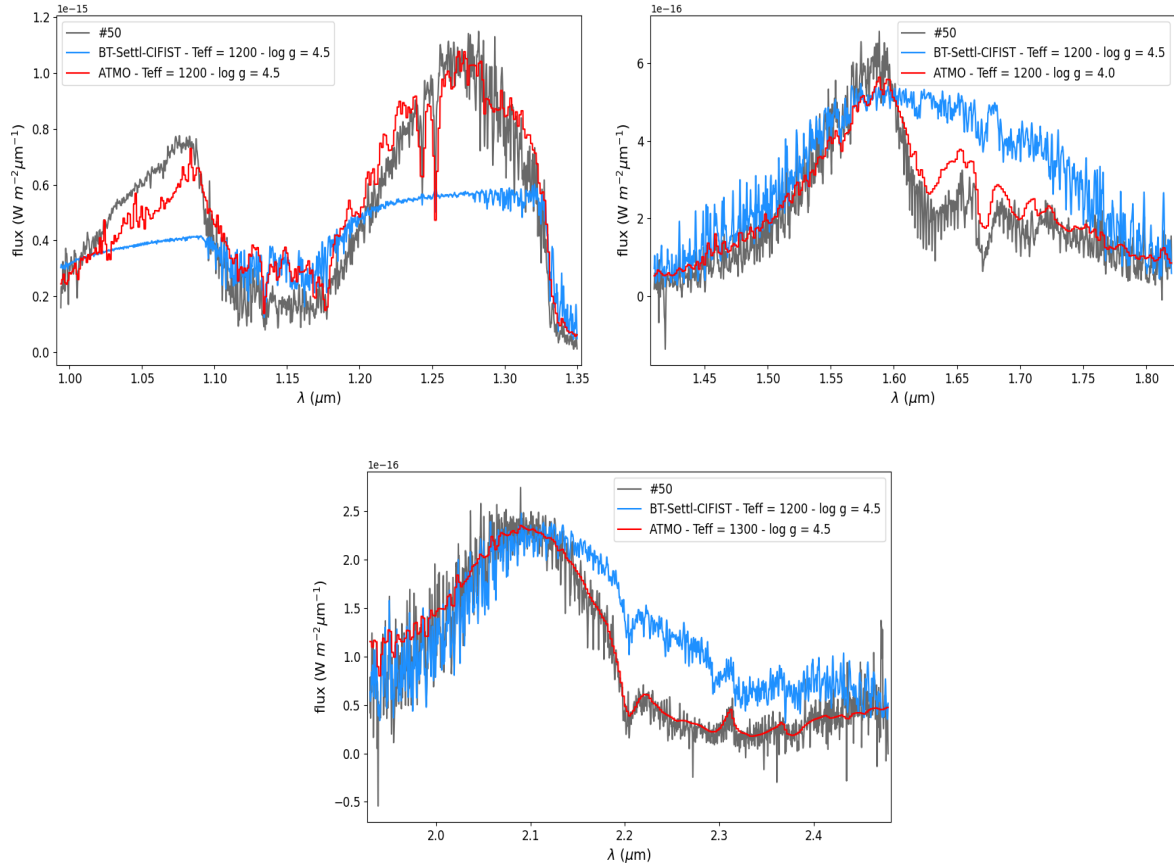
Figure 14: *Three parts of spectrum of object ID #50 shown and fitted separately with best-fits BSC (blue) and ATMO (red) models.*

wavelengths. There is a slight mismatch in the first part of the spectrum, where the model's flux values are higher between the first two object peaks, and the width of the second peak is slightly wider than that of the object.

Figure 14 consistently shows a mismatch for the BSC model across all three parts of the spectrum, even after adjusting for different normalization values and separate best-fit searches. In Figure 14, the ATMO model displays slightly more differences compared to the object. The top left image highlights an offset in the first peak relative to the object's, despite the T_{eff} and log g being the same for both the full spectrum and this part of the spectrum. For the second part of the spectrum, T_{eff} remains the same as for the full spectrum, but the log g is slightly lower, resulting in a divergence in the wavelength range [1.58, 1.7] μm. For the ATMO model, the best-fit for the third part of the spectrum is 1300 K, which is 100 K higher than the full spectrum best-fit but within the expected error range. It matches the object's spectrum excellently, except at the beginning of the range where there is a slight over-prediction of flux.

4.2.5 Model behaviour

From the previous analysis, which included detailed full-spectrum and separate spectrum comparisons for objects of different SpTs, we can draw several conclusions about the model behavior. The BSC model generally provides a better fit for the full spectrum of hotter objects as expected, noting the models key restraints. However, it often overpredicts flux in the first and second parts of the spectrum due to issues with dust opacity. There is also a noticeable underprediction of flux in the third part of the spectrum for some objects, already in [15]. Although the BSC model is extended to a T_{eff} of 1200 K, it struggles to accurately reproduce the spectrum of cooler objects, particularly T-dwarfs, for both full-spectrum and separate spectrum fits. In contrast, the ATMO model excels at matching T-dwarf spectra, achieving accurate full-spectrum and individual best-fits. For both models, separate spectrum fitting yields better alignment with the object's spectrum compared to full-spectrum fitting. However, a drawback of this approach is that it results in different T_{eff} and log g values for different parts of the spectrum for the same object.

4.3 Mass and radius
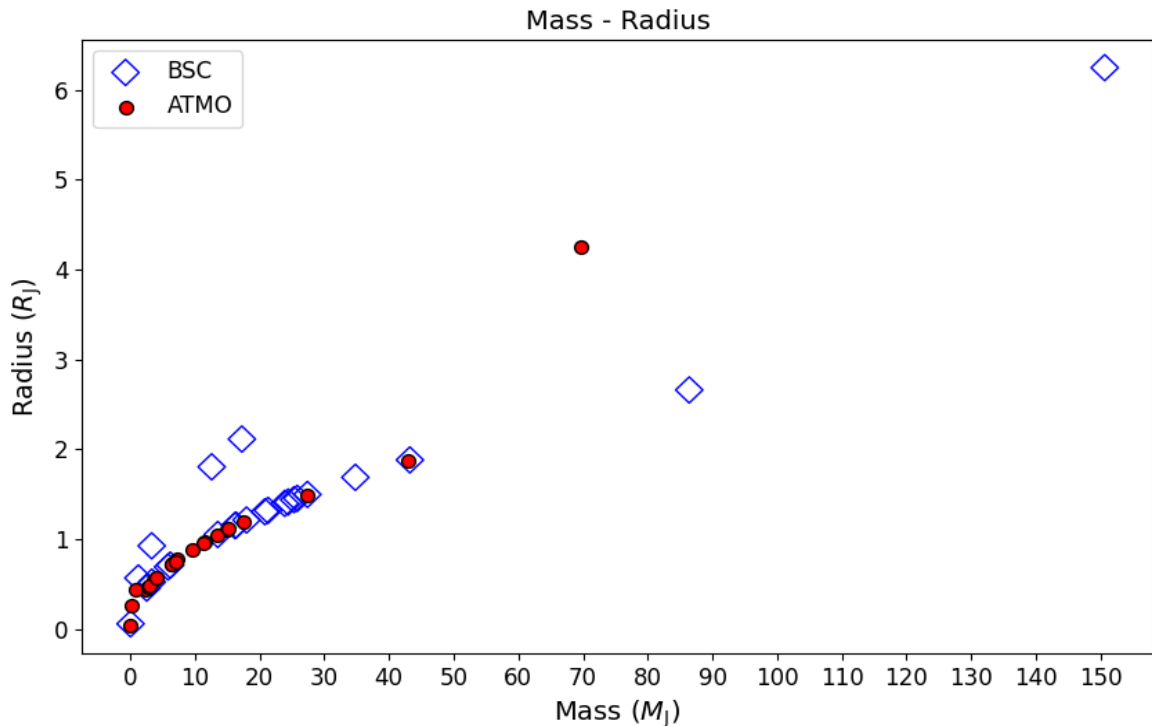
Figure 15: *Dependence of objects mass and radius calculated using best-fit T_{eff} and log g obtained for models BSC, represented as blue diamonds, and ATMO, represented as red circles.*

The objects studied in this work do not undergo hydrogen fusion, setting an upper mass limit of approximately 75 M_J. Given that most of these objects are L-type, with only two being T-type, the expected mass for these spectral types is greater than 3 M_J [15]. The radius
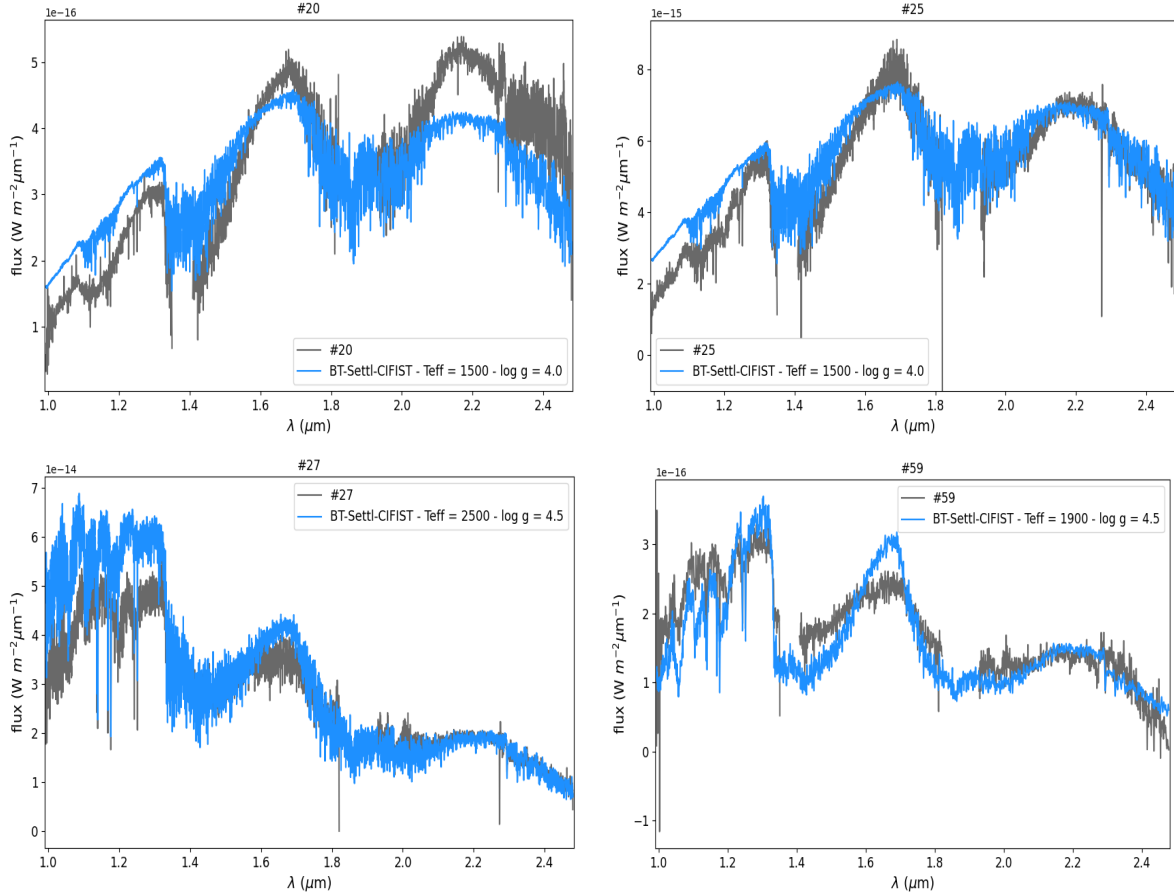
Figure 16: *Spectrum of objects ID #20, #25, #27 and #59, whose masses are below 3 M_J, with BSC model spectrum at best-fit T_{eff} and log g to indicate the spectrum and model behavior to withdraw conclusions about the mass and radius.*

and mass values calculated for both models and corresponding errors are stated in appendix C in Table 5. Figure 15 illustrates the relationship between mass and radius for both models. The graph generally follows the relation $M \sim R^2$, with some exceptions due to age-related variations. There are a few objects with nonphysical masses for brown dwarfs, below 3 M_J for both BSC and ATMO, including one notable case, ID #60, which exhibits an unusually large mass of 150 M_J and a radius exceeding 6 R_J in the BSC model, and 70 M_J with a radius of 4 R_J in the ATMO model. This object, classified as SpT L1.0 ± 0.5, falls within the M/L transition region, which displays the spectrum mismatch with the BSC model, resulting in an abnormally large mass. Furthermore, as previously noted, the ATMO model struggles with predicting and matching the spectra of hotter objects, which likely contributes to the anomalous mass calculations. Figure 16 displays the spectra for objects ID #20 and ID #25, which show a specific spectrum similar to object ID #47 and thus have the same best-fit T_{eff} of 1500 K and log g of 4.0, with flattening in the first part but altogether more pronounced peaks and amplitude differences. Object ID #20 with SpT of L4.5 has a spectrum that deviates significantly from the model's best fit, influencing dilution factor value. This results in a small radius of 0.569 R_J and a mass of 1.2 M_J. For object ID #25, there is a relatively good match with the model spectrum,
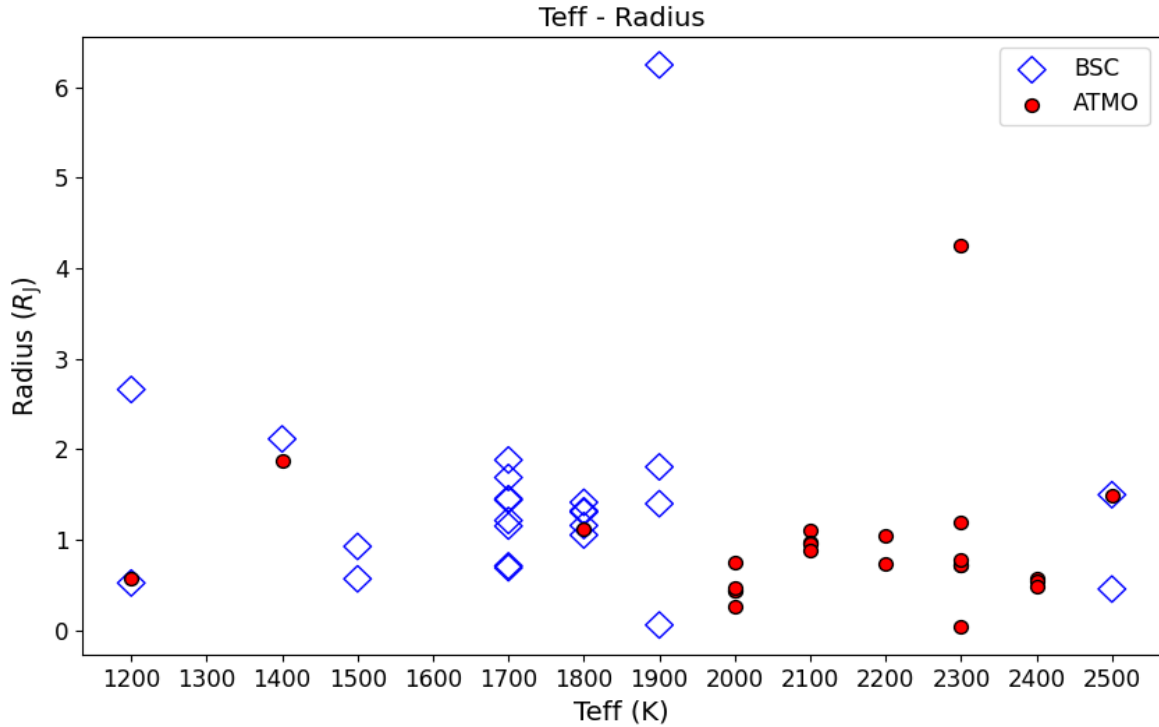
Figure 17: *Dependence of best-fit* T_{eff} *and calculated radius using both models BSC, represented as blue diamonds, and ATMO, represented as red circles.*

aside from differences in the first and second parts. Given its classification as SpT L2.5 $\pm$ 1.0 and its proximity to the M/L transition, the lower-than-expected best-fit T_{eff} suggests that issues with model dust opacity may be causing the misalignment. Despite its mass being just above the expected lower mass limit, the low best-fit T_{eff} contributes to the faulty mass calculation. In Figure 16, the spectrum of object ID #27 is severely overpredicted in the first part by the BSC model, likely due to its position in the M/L transition region, it's radius is due to that 0.455 and mass 2.5 M_J. Additionally, Figure 16 reveals a significant discrepancy between the spectrum of object ID #59 and the BSC best-fit, particularly in the first and second parts of the spectrum, characteristic of the M/L transition. The abnormally small radius and even smaller mass are probably directly linked to the large peak difference of the object and the model, in the second part of spectrum, influencing dilution factor and thus radius.

Figure 17 displays the radius, while Figure 18 shows the mass, and their dependence on the best-fit T_{eff} for the BSC model (blue diamonds) and the ATMO model (red circles). As discussed in Section 4.1, the BSC model tends to cluster objects at temperatures around 1700-1800 K. For these objects, the radius generally ranges from 1 to 2 R_J, and the mass ranges from 10 to 45 M_J, with two exceptions having a radius of approximately 0.7 R_J and a mass of around 6 M_J, both corresponding to the SpT of L4. Given the ATMO model's excellent fit for T-dwarfs, we consider the radius and mass of objects at 1200 K and 1400 K to be reasonably accurate. For example, object ID #50, with a SpT of T5.5, has a radius of 0.523 R_J and a mass of 3.3 M_J, while ID #56, with a SpT of T2, has a radius of 1.896 R_J and a mass of 43.9 M_J. Figure 15

24
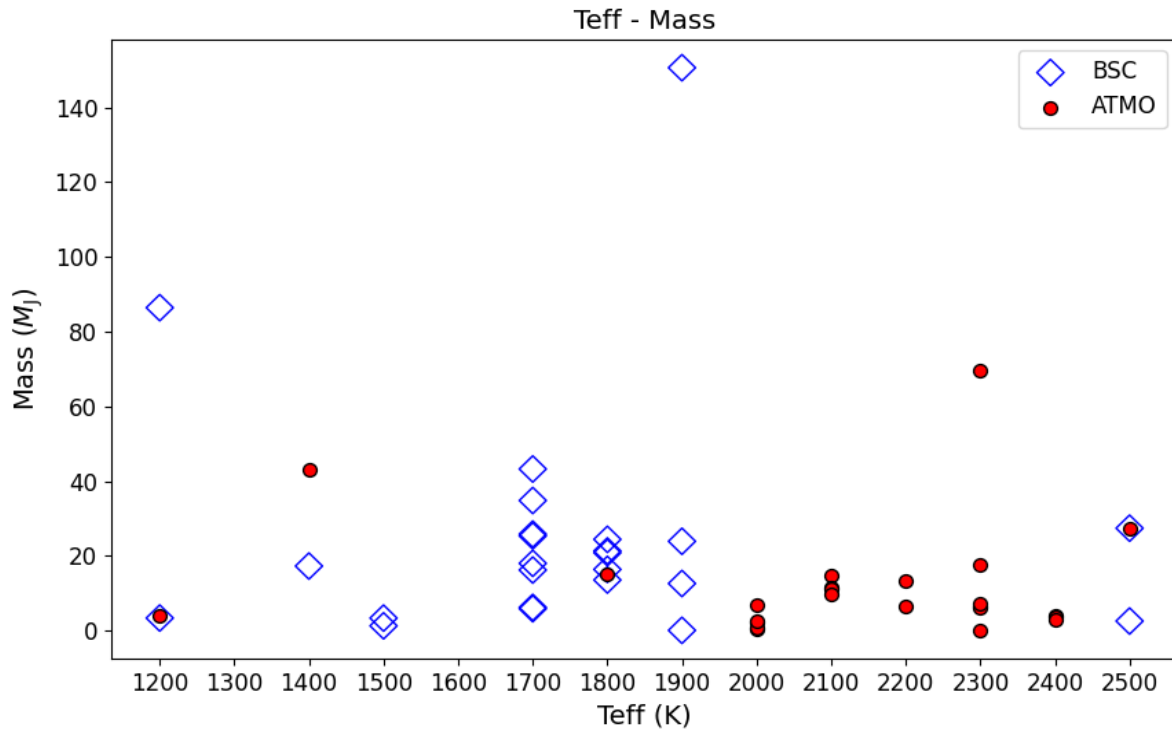
Figure 18: *Dependence of best-fit* T_{eff} *and calculated mass using both models BSC, represented as blue diamonds, and ATMO, represented as red circles.*

illustrates the mass difference for the objects as calculated by the BSC and ATMO models. The primary distinction between the models is that the ATMO model consistently yields smaller mass values than the BSC model. The scale of the x-axis, showing the masses for the ATMO model, is half the length of the y-axis, which represents masses for the BSC model. Only one object, ID #37 (SpT L0.5 $\pm$ 0.5), diverges by having a higher mass as calculated by the ATMO model.

In the study by [14], the authors compared the radius findings of the BSC model with an evolutionary model for their dataset. They found that the BSC model tends to overestimate the radius by approximately 1.5 R_J for objects in the M/L transition, which also leads to an overestimation of mass, and it underestimates the radius by 0.1 to 0.7 R_J for objects later than L3. This also contributes to the small radius and mass calculation of the previously highlighted objects.
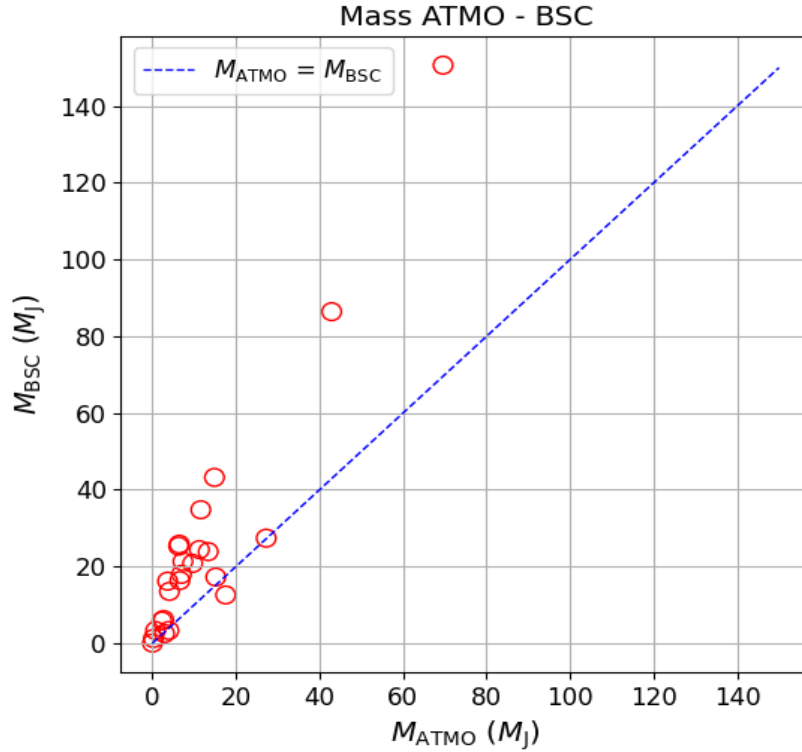
Figure 19: *Difference of objects mass calculated using best-fit* T_{eff} *and log g obtained for models ATMO and BSC.*

5   Conclusions

In this study, we characterized 34 objects as classified in [8]. Determining the T_{eff} and log *g* is crucial for estimating the mass and radius of these objects. The best-fit T_{eff} and log *g* values were obtained by comparing the observed spectra with model spectra in the NIR wavelengths, using the least squares minimization method. This comparison was performed for the full spectrum as well as for three separate spectral regions to assess model behavior and spectrum matching. The BSC and ATMO models were used for spectral comparison. The resulting values were then used to calculate the mass and radius of the objects according to both models.

1. Firstly we analyzed the spectral characteristics and atomic and molecular lines in three of our objects whith SpT from early L-type, middle L-type and T-type, respectively. From that we found that in the J-band, the characteristic atomic lines NaI and KI doublets, which are most prominent, were identified in the spectra of objects with spectral type L, while only the KI doublet at 1.25 μm appeared in the T-dwarf spectra. The FeI line at 1.189 μm is visible in early L type dwarfs but diminishes in the later L- and T-type dwarfs. In the H-band, T-dwarfs exhibit a broad CH_4 absorption line at 1.67 μm. While a KI line at 1.516 μm was expected, the early L type object ID #23 displayed only a weak line. The K-band is characterized by five CO lines, which are prominent in L type dwarfs. However, the early L type object #23 lacks lines at 2.383 and 2.414 μm, while the later L type object #48 lacks

26

lines at 2.323 and 2.414 μm.

2. Comparison with the BSC and ATMO models yielded best-fit T_{eff} values for both the full spectrum and individual spectral regions for all objects. The BSC model tends to cluster objects around T_{eff} values of 1700 K and 1800 K, showing a noticeable gap in the 2000 K – 2400 K range when considering the full-spectrum best-fit. In contrast, the ATMO model generally assigns higher temperatures to L-type objects, typically exceeding 2000 K. Additionally, the best-fit temperatures for individual spectral regions in both models often deviated from the full-spectrum best-fit by an average of 200 K.

3. In a detailed comparison of four selected objects, the BSC model consistently failed to reproduce the shape of the H-band of the spectrum for L-type dwarfs and overpredicted the flux in the J-band, likely due to the inclusion of dust opacity in the model. It also struggled to accurately represent the T-dwarf spectrum. In contrast, the ATMO model was unable to replicate the L-type spectrum but showed excellent alignment with the T-type dwarf spectrum.

4. Mass calculations using the BSC model generally returned values above 3 M_J, with some falling below this threshold. For PMO-s, the mass is expected to be below the deuterium-burning limit, but our calculations identified two objects, #21 and #26, with masses above 3 M_J, which we consider plausible. There are four objects with masses below this limit, possibly due to inaccuracies in the model. The calculated radii are mostly around 1 or 2 R_J, with six objects having radii below 1 R_J, all of which have masses below 10 M_J. This could be due to the model underestimating the radius for early L-type spectral objects, to which these belong. In this analysis we did not take in the account mass and radius calculations for T-dwarfs using BSC model. On the other hand, the ATMO model showed mismatches when fitting L-dwarf spectra, suggesting that its mass calculations for these hotter objects are likely incorrect. However, the mass estimates for T-dwarfs appear to be more reliable.

Adjustments and refinements in models can improve the accuracy of aligning with observed data across different spectral segments and better mass and radius calculations. While the models provide the best predictions for these objects, they do not perfectly represent all atmospheric effects and processes. Thus, the fit is not perfect, but it offers an insight into the potential conditions and processes occurring on these objects.

6 Bibliography

[1] José A. Caballero: *A Review on Substellar Objects below the Deuterium Burning Mass Limit: Planets, Brown Dwarfs or What?*, Geosiences, **8**, 10, 2018.
DOI: https://doi.org/10.1051/0004-6361/202347327

[2] I. Neill Reid and Suzanne L. Hawley: *New Light on Dark Stars: Red Dwarfs, Low-Mass Stars, Brown Dwarfs*, Springer Berlin, Heidelberg, 2005.

[3] M. W. Phillips, P. Tremblin, I. Baraffe, G. Chabrier, N. F. Allard, F. Spiegelman, J. M. Goyal, B. Drummond and E. Hébrard: *A new set of atmosphere and evolution models for cool T–Y brown dwarfs and giant exoplanets*, Astronomy and Astrophysics manuscript, **637**, A38, 2020.
DOI: https://doi.org/10.1051/0004-6361/201937381

[4] M.S. Marley and T.D. Robinson: *On the Cool Side: Modeling the Atmospheres of Brown Dwarfs and Giant Planets*, The Annual Review of Astronomy and Astrophysics, textbf53, 279-323, 2015. DOI: 10.1146/annurev-astro-082214-122522

[5] France Allard, Tristan Guillot, Hans-Gunter Ludwig, Peter H. Hauschildt, Andreas Schweitzer, David R. Alexander and Jason W. Ferguson: *Model Atmospheres and Spectra: The Role of Dust*, Symposium - International Astronomical Union, **211**, 325-332, 2003. DOI: 10.1017/S0074180900210875

[6] H. Buoy et. al: *Infrared spectroscopy of free-floating planet candidates in Upper Scorpius and Ophiuchus*, Astronomy and Astrophysics, **664**, A111, 2022.
DOI: https://doi.org/10.1051/0004-6361/202243850

[7] Núria Miret-Roig et. al: *A rich population of free-floating planets in the Upper Scorpius young stellar association*, Nature Astronomy, **6**, 89-97, 2022. DOI: https://doi.org/10.1038/s41550-021-01513-x

[8] L. Piscarreta, K. Mužić, V., Almendros-Abad and A. Scholz: *Spectral characterization of young LT dwarfs*, Astronomy and Astrophysics manuscript, **686**, A37, 2024.
DOI: https://doi.org/10.1051/0004-6361/202347327

[9] Michael C. Cushing, Jhon T. Rayner, William D. Vacca: *An infrared spectroscopic sequence of M, L and T dwarfs*, The Astrophysical Journal, **623**, 1115-1140, 2005.
DOI: https://doi.org/10.1086/428040

[10] Elena Manjavacas, Pascal Tremblin, Stephan Birkmann, Jeff Valenti, Catarina Alves de Oliveira, Tracy L. Beck, G. Giardino, N. L¨utzgendorf, B. J. Rauscher, and M. Sirianni: *Medium Resolution 0.97-5.3 μm spectra of Very Young Benchmark Brown Dwarfs with*

NIRSpec onboard the James Webb Space Telescope, The Astronomical Journal, **167**(4):168, 2024.
DOI: 10.3847/1538-3881/ad2938

[11] France Allard, Peter H. Hauschildt, David R. Alexander, Akemi Tamanai, and Andreas Schweitzer: *The Limiting Effects of Dust in Brown Dwarf Model Atmospheres*, The Astrophysical Journal, **556**, 357, 2001.
DOI: 10.1086/321547

[12] F. Allard, D. Homeier, B. Freytag and C.M. Sharp: *Atmospheres From Very Low-Mass Stars to Extrasolar Planets*, EAS Publications Series, **57**, 3-43, 2012.
DOI: https://doi.org/10.1051/eas/1257001

[13] E. Caffau, H.-G. Ludwig, M. Steffen, B. Freytag, P. Bonifacio: *Solar Chemical Abundances Determined with a CO5BOLD 3D Model Atmosphere*, Solar Physics, **268**, 255–269, 2011.
DOI: https://doi.org/10.1051/eas/1257001

[14] Aniket Sanghi et. al: *The Hawaii Infrared Parallax Program. VI. The Fundamental Properties of 1000+ Ultracool Dwarfs and Planetary-mass Objects Using Optical to Mid-infrared Spectral Energy Distributions and Comparison to BT-Settl and ATMO 2020 Model Atmospheres*, The Astrophysical Journal, **959**, 63, 2023.
DOI: 10.3847/1538-4357/acff66

[15] Spencer A. Hurt, Michael C. Liu, Zhoujian Zhang, Mark Phillips, Katelyn N. Allers, Niall R. Deacon, Kimberly M. Aller, and William M. J. Best: *Uniform Forward-modeling Analysis of Ultracool Dwarfs. III. Late-M and L-Dwarfs in Young Moving Groups, the Pleiades, and the Hyades*, The Astrophysical Journal, **961**, 121, 2024.
DOI: 10.3847/1538-4357/ad0b12

[16] A. Vallenari et. al:*Gaia Data Release 3. Summary of the content and survey properties*, Astronomy & Astrophysics, **674**, A1, 2023.
DOI: https://doi.org/10.1051/0004-6361/202243940

[17] Michael C. Liu, Trent J. Dupuy and Katelyn N. Allers: *The Hawaii Infrared Parallax Program. II. Young Ultracool Field Dwarfs*, The Astrophysical Journal, **833**, 96, 2016.
DOI: 10.3847/1538-4357/833/1/96

[18] A. G. A. Brown et. al: *Gaia Data Release 2. Summary of the contents and survey properties*, Astronomy & Astrophysics, **616**, A1, 2018.
DOI: https://doi.org/10.1051/0004-6361/201833051

[19] William M. J. Best, Michael C. Liu, Eugene A. Magnier, and Trent J. Dupuy: *A Volume-limited Sample of Ultracool Dwarfs. I. Construction, Space Density, and a Gap in the L/T Transition*, The Astronomical Journal, **161**, 42, 2021.
DOI: 10.3847/1538-3881/abc893

[20] P. A. B. Galli, E. Moraux, H. Bouy, J. Bouvier, J. Olivares, and R. Teixeira: *A revised moving cluster distance to the Pleiades open cluster*, Astronomy and Astrophysics, **598**, A48, 2017.
DOI: https://doi.org/10.1051/0004-6361/201629239

[21] Elena Manjavacas et. al:*Cloud Atlas: Hubble Space Telescope Near-infrared Spectral Library of Brown Dwarfs, Planetary-mass Companions, and Hot Jupiters*, The Astronomical Journal, **157**, 101, 2018.
DOI: 10.3847/1538-3881/aaf88f

A Parallax

In Table 2 we give parallax values and corresponding errors from [8].

Table 2: *Parallax and corresponding error of the objects which is used to calculate the distance.*

Object	Parallax [mas]	Error parallax [mas]	Reference
19	28.9542	0.4217	[16]
20	45.1	1.7	[17]
21	32.6	1.0	[17]
23	65.9	1.3	[17]
24	18.2843	0.5866	[16]
25	109.1381	0.4833	[16]
26	86.4	0.8	[17]
27	155.9	1.0	[17]
31	23.3266	0.9593	[16]
32	23.1731	0.1957	[16]
33	20.6433	0.8084	[16]
34	25.1685	0.4443	[16]
35	23.4134	0.6966	[16]
36	27.4375	0.5455	[18]
37	21.2769	0.2888	[16]
38	25.5625	0.7130	[18]
39	18.5	2.1	[17]
46	15.2341	0.9558	[16]
50	52.1	1.2	[17]
51	43.3	6.2	[19]
56	162.1	0.6	[19]
59	7.6	1.2	[20]
60	7.9	1.3	[20]
61	26.4742	0.2539	[16]
62	49.6	2.8	[19]
63	21.00	0.07	[21]

B Effective temperature and surface gravity data

In Table 3 we state best-fit T_{eff} and log g calculated with ATMO model for the full spectrum and the three parts of spectra for each object.

Table 3: *Best-fit T_{eff} and log g for BSC model for the whole spectra and parts of spectra, written with indices 1,2 and 3, respectively.*

Object	T_{eff} [K]	log g	$T_{eff\,1}$ [K]	log g_1	$T_{eff\,2}$ [K]	log g_2	$T_{eff\,3}$ [K]	log g_3
19	1800	4.5	2100	4.0	1500	4.5	2400	4.5
20	1500	4.0	1700	4.5	1600	4.0	1600	4.0
21	1700	4.5	1700	4.0	1700	4.5	1800	4.5
23	1700	4.5	2100	4.0	1600	4.5	2500	4.5
24	1700	4.5	1700	4.5	1600	4.5	2400	4.5
25	1500	4.0	1700	4.0	1600	4.0	1600	4.0
26	1700	4.5	1700	4.5	1400	4.0	1800	4.5
27	2500	4.5	2300	4.0	2600	4.5	2600	4.5
28	1400	4.0	1700	4.5	1400	4.0	1700	4.0
29	1700	4.5	1800	4.5	1400	4.0	2400	4.5
31	1800	4.5	1900	4.0	1700	4.5	2400	4.5
32	2500	4.5	2300	4.0	2600	4.0	2500	4.5
33	1700	4.5	2200	4.0	1600	4.5	2500	4.0
34	1700	4.5	1700	4.5	1600	4.5	2500	4.0
35	1700	4.5	1900	4.0	1600	4.5	2500	4.0
36	1800	4.5	2100	4.0	1600	4.5	2500	4.5
37	1900	4.0	2200	4.0	2500	4.0	2500	4.5
38	1800	4.5	1900	4.0	1700	4.5	2600	4.0
39	1800	4.5	2100	4.0	1600	4.5	2500	4.5
40	1700	4.5	1800	4.5	1700	4.5	2500	4.5
41	1700	4.5	1800	4.5	1700	4.5	1800	4.5
42	1700	4.5	1700	4.5	1700	4.5	1900	4.0
46	1900	4.5	1600	4.0	2500	4.5	2500	4.5
47	1500	4.0	1700	4.5	1600	4.0	1700	4.5
48	1600	4.0	1700	4.5	1700	4.5	1700	4.0
49	1800	4.5	2200	4.0	1400	4.0	2400	4.0
50	1200	4.5	1200	4.0	1200	4.5	1200	4.5
56	1200	4.5	1200	4.0	1200	4.5	1300	4.5
57	1900	4.5	2100	4.0	2600	4.5	2500	4.5
58	1400	4.5	2200	4.0	1400	4.5	2500	4.5
59	1900	4.5	2100	4.0	2600	4.5	2500	4.0
60	1700	4.5	1400	4.5	1400	4.0	2400	4.0
61	1900	4.0	2200	4.0	1600	4.5	2500	4.5
62	1400	4.0	1800	4.5	1400	4.0	1900	4.0

In Table 4 we state best-fit T_{eff} and log g calculated with ATMO model for the full spectrum and the three parts of spectra for each object.

Table 4: *Best-fit* T_{eff} *and log g for ATMO model for the whole spectra and parts of spectra, written with indices 1,2 and 3, respectively.*

Object	T_{eff} [K]	log g	$T_{eff\,1}$ [K]	log g_1	$T_{eff\,2}$ [K]	log g_2	$T_{eff\,3}$ [K]	log g_3
19	2400	4.5	1900	4.5	2400	4.0	2400	4.5
20	2000	4.0	1800	4.0	2300	4.0	2100	4.5
21	2000	4.5	1600	4.0	2200	4.0	2100	4.5
23	2400	4.5	1800	4.5	2400	4.0	2400	4.5
24	2100	4.5	1900	4.0	2400	4.0	2300	4.0
25	2000	4.0	1600	4.0	2300	4.0	2300	4.0
26	2000	4.5	1900	4.0	2200	4.5	2200	4.5
27	2400	4.5	2200	4.5	2500	4.5	2500	4.5
28	2000	4.5	1800	4.0	2200	4.5	2100	4.0
29	2000	4.5	1700	4.0	2300	4.5	2200	4.0
31	2200	4.5	1700	4.5	2300	4.0	2200	4.0
32	2500	4.5	2200	4.5	2600	4.5	2400	4.5
33	2300	4.5	1900	4.0	2400	4.0	2400	4.0
34	2100	4.5	1900	4.0	2400	4.0	2400	4.0
35	2300	4.5	1700	4.5	2400	4.0	2400	4.0
36	2100	4.5	1800	4.0	2400	4.0	2300	4.0
37	2300	4.5	1900	4.0	2500	4.5	2400	4.5
38	2100	4.5	1700	4.5	2300	4.0	2400	4.0
39	2300	4.5	1900	4.5	2400	4.0	2400	4.0
40	2100	4.5	1800	4.0	2400	4.5	2300	4.0
41	2100	4.5	1700	4.0	2300	4.0	2200	4.5
42	2000	4.5	1800	4.0	2300	4.0	2200	4.0
46	2200	4.5	2100	4.0	2400	4.5	2400	4.5
47	1900	4.0	1800	4.0	2300	4.0	2000	4.5
48	1900	4.0	1900	4.0	2100	4.0	2000	4.0
49	2200	4.5	1900	4.0	2400	4.5	2400	4.0
50	1200	4.5	1200	4.5	1200	4.5	1300	4.5
56	1400	4.5	2100	4.0	1400	4.5	1500	4.5
57	2300	4.5	1900	4.5	2600	4.5	2400	4.5
58	2100	4.5	1900	4.5	2600	4.5	2400	4.5
59	2300	4.5	1900	4.5	2500	4.5	2400	4.0
60	2000	4.5	2400	4.0	2400	4.5	2400	4.0
61	2300	4.0	1900	4.0	2400	4.0	2300	4.0
62	1800	4.5	1700	4.0	2200	4.5	2200	4.0

C Mass and radius data

Table 5 shows objects spectral type along with mass and radius with corresponding errors calculated with both models. Here we also note SpTs for all objects from [8], for easier comparison of mass and radius values between different SpTs.

Table 5: *Objects mass and radius and corresponding errors calculated using the best-fit* T_{eff} *and log g for both models, BSC and ATMO.*

		BSC		ATMO	
Object	SpT	$R\,[R_J]$	$M\,[M_J]$	$R\,[R_J]$	$M\,[M_J]$
19	L1.0	1.0527 ± 0.0153	13.5 ± 15.6	0.5733 ± 0.0083	4.0 ± 4.6
20	L4.5	0.5685 ± 0.0214	1.2 ± 1.4	0.2660 ± 0.0100	0.273 ± 0.315
21	L4.5	0.6910 ± 0.0212	5.8 ± 6.7	0.4378 ± 0.0134	2.3 ± 2.7
23	L1.5	1.1517 ± 0.0227	16.2 ± 18.6	0.5441 ± 0.0107	3.6 ± 4.2
24	L1.0	1.8823 ± 0.0604	43.2 ± 49.8	1.1158 ± 0.0358	15.2 ± 17.5
25	L2.5	0.9267 ± 0.0041	3.3 ± 3.8	0.4576 ± 0.0020	0.808 ± 0.930
26	L4.0	0.7121 ± 0.0066	6.2 ± 7.1	0.4699 ± 0.0044	2.7 ± 3.1022
27	M9.5	0.4557 ± 0.0029	2.5 ± 2.9	0.4842 ± 0.0031	2.9 ± 3.2938
31	L2.5	1.1578 ± 0.0476	16.4 ± 18.9	0.7525 ± 0.0309	6.9 ± 7.9736
32	L0.0	1.4981 ± 0.0127	27.4 ± 31.5	1.4981 ± 0.0127	27.4 ± 31.5
33	L1.0	1.4545 ± 0.0570	25.8 ± 29.8	0.7079 ± 0.0277	6.1 ± 7.1
34	L0.5	1.6887 ± 0.0298	34.8 ± 40.1	0.9872 ± 0.0174	11.9 ± 13.7
35	L0.5	1.4404 ± 0.0429	25.3 ± 29.2	0.6989 ± 0.0208	6.0 ± 6.9
36	L1.0	1.4141 ± 0.0281	24.4 ± 28.1	0.9716 ± 0.0193	11.5 ± 13.3
37	L0.5	1.8057 ± 0.0245	12.6 ± 14.5	1.1712 ± 0.0159	16.7 ± 19.3
38	L2.5	1.3061 ± 0.0364	20.8 ± 24.0	0.8988 ± 0.0251	9.9 ± 11.4
39	L1.0	1.3211 ± 0.1500	21.3 ± 25.0	0.7554 ± 0.0858	7.0 ± 8.2
46	L1.0	1.3990 ± 0.0878	23.9 ± 27.7	1.0739 ± 0.0674	14.1 ± 16.3
50	T5.5	0.5227 ± 0.0120	3.3 ± 3.8	0.5227 ± 0.0120	3.3 ± 3.8
56	T2.0	2.6613 ± 0.3811	86.4 ± 102.5	1.8962 ± 0.2715	43.9 ± 52.0
59	L1.0	0.0583 ± 0.0002	0.042 ± 0.048	0.0393 ± 0.0001	0.019 ± 0.022
60	L2.5	1.2136 ± 0.1916	18.0 ± 21.5	0.7639 ± 0.1206	7.1 ± 8.5
61	L1.0	6.2486 ± 1.0282	150.6 ± 180.4	4.2787 ± 0.7041	70.6 ± 84.6
62	L5.0	2.1146 ± 0.0203	17.3 ± 19.9	1.2600 ± 0.0121	19.4 ± 22.3